POLITECNICO DI TORINO

**MASTER OF SCIENCE IN ELECTRICAL ENGINEERING**

MASTER'S DEGREE THESIS

# Experimental performance evaluation of a fractional power induction machine at ambient and cryogenic temperatures


**Academic Supervisors**
Prof. Silvio Vaschetto
Prof. João Filipe Pereira Fernandes
Eng. Inês Santos Perdigão Peixoto

**Candidate**
Enrico Panero

Academic Year 2022-2023

Alla mia famiglia, ai miei amici, ai miei professori, agli incontri casuali, a tutti coloro che mi hanno guidato nella vita.

*"Be yourself, everyone else is already taken"*
*Oscar Wilde*

# Contents


Abstract . . . .

**1 Introduction** **1**

1.1 Cryogenic Machines Overview . . . . 2

1.1.1 Cryogenic Coolants . . . . 2

1.1.2 Advantages of Cryogenic Operations . . . . 3

1.1.3 Disadvantages of Cryogenic Operations . . . . 4

1.2 Superconducting Electric Machines . . . . 4

1.3 Early Applications . . . . 6

1.4 Future Trends . . . . 8

1.4.1 Electrification of Aircraft . . . . 8

1.4.2 Naval Propulsion . . . . 9

1.5 Goal of the Thesis . . . . 11

**2 Ambient Tests** **12**

2.1 Standard Tests on Induction Motors . . . . 12

2.1.1 Winding Resistance . . . . 12

2.1.2 No-load Test . . . . 12

2.1.3 Locked Rotor Test . . . . 13

2.1.4 Load Test . . . . 13

2.2 Induction Motor Electromechanical Model . . . . 14

2.3 Motor Under Test and Measurement Devices . . . . 15

2.4 No-load Ambient Test . . . . 16

2.5 Locked Rotor Ambient Test . . . . 20

2.6 Load Ambient Test . . . . 23

2.6.1 DC Machine Characterization . . . . 24

2.6.2 Experimental Setup . . . . 26

2.6.3 Theoretical Analysis . . . . 28

2.6.4 Results . . . . 30

2.7 Comparison with a Similar Motor . . . . 36

2.7.1 No-load and Locked Rotor Test Comparison . . . . 36

2.7.2 Load Test Comparison . . . . 37

**3 Cryogenic Tests** **41**
3.1 No-load and Locked Rotor Test . . . 43
3.1.1 No-load Cryogenic Test . . . 43
3.1.2 Locked Rotor Cryogenic Test . . . 46
3.1.3 Results . . . 47
3.2 Load Cryogenic Test . . . 48
3.2.1 Results . . . 50
3.3 Room vs Cryogenic Temperature Comparison . . . 55
3.3.1 Torque and Power . . . 55
3.3.2 Efficiency . . . 59
3.4 Comparison with a Similar Motor . . . 60

**4 Additional Load Losses** **63**
4.1 Theoretical Overview . . . 63
4.1.1 Physical Phenomena Underlying Stray Load Losses . . . 63
4.1.2 Efficiency and Losses Estimation According to Different Standards . . . 64
4.2 Experimental Results at Cryogenic Temperature . . . 65

**5 Conclusions and Future Works** **69**
5.1 Conclusions . . . 69
5.2 Future Works . . . 70
Appendix . . .

# Abstract

The need for energy-saving solutions in electric machines design is growing because of environmental concerns. Cryogenic cooling offers benefits to electric motors, especially in terms of efficiency, torque and power density. While not typically available in conventional applications, some particular applications such as natural gas pumping and future electric aircraft may benefit from these advantages.

A conventional three phase 90W induction motor was tested in standard conditions and immersed in a liquid nitrogen environment to study the difference in performance and the variation of the parameters of the equivalent single phase circuit.

The results have shown that in the cryogenic environment, the mechanical and iron losses are higher. However, a significant reduction in Joule losses has been observed. This led to an overall increase in motor efficiency by +26.8%. Additionally, the motor displayed a +51.6% increase in torque and a +69.6% increase in power output under cryogenic conditions. For validation, the motor under test has been compared with a similar 90W induction motor previously tested. The results from both motors aligned closely, thus reinforcing the reliability of the data. The tests on a bigger 550W induction motor, moreover, have shown the same trend in performance and parameters variation.

Lastly, an overview of the stray load losses in cryogenic conditions for the two 90W motors has been provided.

# List of Figures


1.1 Estimated share of global electricity demand by end use . . . 1
1.2 Estimated electricity demand for all electric motors by sector . . . 2
1.3 Typical submerged cooling system of an electric motor . . . 3
1.4 Different shapes of HTS bulk superconductors . . . 5
1.5 Second Generation (2G) HTS YBCO tape superconductor . . . 5
1.6 Cryogenic submerged pumps for liquified natural gas (LNG) by Vanzetti Engineering . . . 7
1.7 Submerged pump assembly for LNG applications using a cryogenic-cooled induction machine . . . 7
1.8 Aircrafts evolution: from conventional to more electric . . . 8
1.9 ASCEND (Advanced Superconducting and Cryogenic Experimental powertraiN Demonstrator) . . . 9
1.10 An example of Hybrid Diesel–Turbo-Electric configuration . . . 10
1.11 Instituto Superior Técnico Lisboa . . . 11

2.1 Single phase equivalent circuit of an induction motor . . . 14
2.2 Picture of the induction motor under test . . . 15
2.3 NI measurement device and conditioning circuit . . . 16
2.4 Electrical schematic for the measurement of the stator resistance . . . 16
2.5 No-load ambient test: input power, copper losses, mechanical and iron losses 17
2.6 No-load ambient test: mechanical and iron losses as a function of the magnetizing voltage . . . 18
2.7 No-load ambient test: reactive power as a function of the magnetizing voltage 18
2.8 Phasor diagram illustrating the stator voltage and current . . . 19
2.9 Locked rotor ambient test: input active power as a function of the stator current 21
2.10 Locked rotor ambient test: input reactive power as a function of the stator current . . . 21
2.11 Electric resistivity of copper as function of the temperature . . . 22
2.12 DC Machine equivalent circuit . . . 24
2.13 Armature constant of the DC Machine . . . 25
2.14 Mechanical and iron losses map as function of the rotor speed and field current 26
2.15 Load test electrical schematic . . . 26

2.16 Ambient load test experimental setup . . . 27
2.17 Load test power chain . . . 27
2.18 Single phase equivalent circuit simplification step 1 . . . 28
2.19 Single phase equivalent circuit simplification step 2 . . . 29
2.20 Speed vs torque characteristic as function of the voltage . . . 30
2.21 Speed vs torque ambient characteristics - analytical curve and experimental points . . . 31
2.22 Speed vs torque ambient characteristics - analytical curve and experimental points optimization . . . 32
2.23 Electric resistivity of the aluminum alloy 2024-0 as function of the temperature 33
2.24 Speed vs efficiency ambient characteristics - analytical curve and experimental points . . . 34
2.25 Equivalent circuit of induction motor highlighting the presence of the stator leakage reactance . . . 34
2.26 Speed vs efficiency characteristics considering stator leakage reactance . . . 35
2.27 Speed vs efficiency characteristics as function of the magnetizing reactance . 35
2.28 Comparison of the dimensions of the two 90W induction motors . . . 36
2.29 Speed vs torque ambient characteristics comparison between Motor I and Motor II (MUT) . . . 38
2.30 Speed vs torque ambient characteristics and load test comparison between Motor I and Motor II (MUT) . . . 38
2.31 Speed vs efficiency characteristics comparison . . . 39

3.1 Liquid nitrogen storage cylinder . . . 41
3.2 Grease removal process from the bearings . . . 42
3.3 Ice formations on the motor after removing from LN2 . . . 42
3.4 No-load test setup in cryogenic conditions . . . 43
3.5 Rotor surface smoothing using the sandpaper . . . 44
3.6 No-load cryogenic test: mechanical and iron losses as a function of the magnetizing voltage . . . 45
3.7 No-load cryogenic test: reactive power as a function of the magnetizing voltage 45
3.8 Locked rotor test setup in cryogenic conditions . . . 46
3.9 Locked rotor cryogenic test: input active power as a function of the stator current . . . 47
3.10 Locked rotor cryogenic test: input reactive power as a function of the current 47
3.11 Experimental setup for the cryogenic load test . . . 49
3.12 Mist emerging from the induction motor removed from liquid nitrogen . . . 49
3.13 Skin effect in the speed vs torque plot in cryogenic conditions . . . 50
3.14 Influence of the skin effect on the rotor resistance . . . 51
3.15 Current distribution in the slot layers and related phasor diagram . . . 52
3.16 Squirrel cage rotor design . . . 54

3.17 Speed vs efficiency cryogenic characteristics of Motor II (MUT) . . . . . 54
3.18 Speed vs torque characteristics comparison between room and cryogenic temperature for Motor II (MUT) . . . . . 55
3.19 Speed vs torque characteristics as function of the stator resistance . . . . . 56
3.20 Speed vs torque characteristics as function of the rotor resistance . . . . . 57
3.21 Speed vs output power characteristics comparison between room and cryogenic temperature for Motor II (MUT) . . . . . 58
3.22 Speed vs efficiency characteristics comparison between room and cryogenic temperature for Motor II (MUT) . . . . . 59
3.23 Speed vs torque characteristics comparison between Motor I and Motor II . . 61
3.24 Speed vs efficiency characteristics comparison between Motor I and Motor II (MUT) . . . . . 62

4.1 Residual load losses Motor II (MUT) . . . . . 66
4.2 Residual load losses Motor I . . . . . 67
4.3 Stray load losses comparison between Motor I and Motor II (MUT) . . . . . 68

# List of Tables


1.1 Advantages and disadvantages of cryogenic machines with respect to conventional ones . . . 4
1.2 Performance comparison between conventional and cryogenic machines . . . 6
1.3 Performance comparison between conventional and cryogenic motors for naval propulsion . . . 11

2.1 Motor under test nameplate . . . 15
2.2 Parameters obtained from the no-load test . . . 19
2.3 Stator resistance and temperature before and after the locked rotor test . . . 23
2.4 Parameters obtained from the locked rotor test . . . 23
2.5 Results of the optimization process for the speed vs torque ambient characteristics . . . 33
2.6 Nameplates comparison between Motor I and Motor II (MUT) . . . 36
2.7 Equivalent circuit parameters comparison between Motor I and Motor II (MUT) at ambient conditions . . . 37

3.1 Comparison of the equivalent circuit parameters of Motor II (MUT) in ambient and cryogenic conditions . . . 48
3.2 Comparison of torque values between ambient and cryogenic test . . . 57
3.3 Comparison of output power values between ambient and cryogenic tests . . . 58
3.4 Comparison of efficiency values between ambient and cryogenic tests for Motor II (MUT) . . . 59
3.5 Variation of the parameters of 90W Motor I from ambient to cryogenic conditions 60
3.6 Variation of the parameters of 90W Motor II (MUT) from ambient to cryogenic conditions . . . 60
3.7 Comparison of the equivalent circuit parameters variation . . . 61
3.8 Comparison of performance variation from ambient to cryogenic conditions . . . 62

4.1 Assigned values in stray load losses in IEEE 112 . . . 65

# Chapter 1

# Introduction

Nowadays an estimated 30 million electric motors are yearly purchased by industry, of which 300 million of them are already under exploitation. Electric motors are found in an extensive array of applications such as transportation, manufacturing, residential appliances and renewable energy systems. In the context of the energy transition, these motors play a key role since they account for a significant portion of the global electricity consumption.
As can be seen in Figure 1.1, electric motors use an estimated 46 % of the global electricity demand, with 64% of it located in the industry [1, 2] (Figure 1.2).

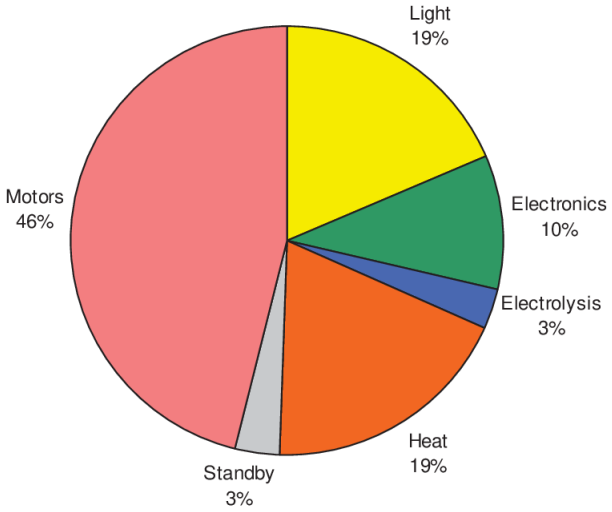


Figure 1.1: Estimated share of global electricity demand by end use

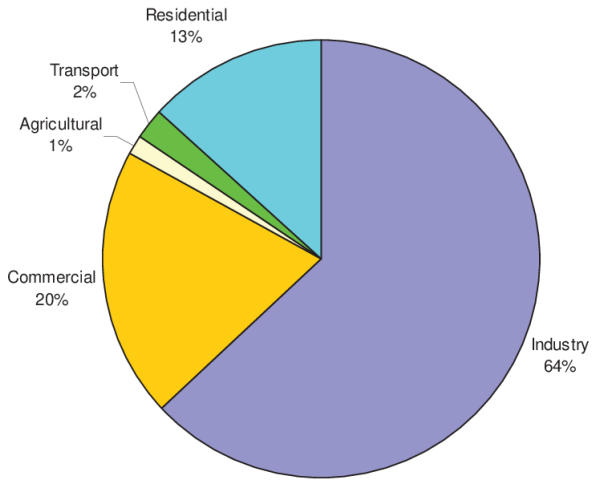


Figure 1.2: Estimated electricity demand for all electric motors by sector

Given the significance of the electricity consumed by electric motors, energy efficiency is considered essential to reduce the economic costs of their exploitation. The estimated electricity saving potential could be 13,360 TWh per year, which coincides with a yearly greenhouse gas emissions reduction of 8579 $t_{CO2eq}$ until 2030 [2].

## 1.1 Cryogenic Machines Overview

Since cryogenic cooling has been shown to improve the performance and efficiency of electric machines and since the world of research and industry has focused on the reduction of CO2 emissions using all-electric solutions with ever-greater efficiencies, these motors represent an interesting field of research.

### 1.1.1 Cryogenic Coolants

By definition, cryogenic electric motors are electric motors that operate in extremely low temperatures, typically below -153°C (120 K). A list of the most common refrigerant fluids is provided below[3]:

- Liquid nitrogen (LN2) exists as a liquid at temperatures below -195.8 °C (77 K). It is relatively inexpensive, abundant, and non-toxic. LN2 can be dangerous to handle, and it requires specialized storage and transfer equipment.
- Liquid Helium (LHe) exists as a liquid at temperatures below -268.9 °C (4.25 K). It is less abundant and more expensive than liquid nitrogen, but it has a much lower boiling point, which makes it useful in applications that require even lower temperatures. At the same time, however, it is more difficult to handle and requires more complex insulation materials.

- Liquid Hydrogen (LH2) exists as a liquid at temperatures below -252.87 °C (20.28 K). It is an efficient coolant and has high thermal conductivity and low viscosity. However, its use must be handled carefully because it is flammable.
- Liquid Neon (LNe) exists as a liquid at temperatures below -246 °C (27 K). It is similar to liquid helium and liquid hydrogen in terms of cooling performance.

The cryogenic or cooling operation may be accomplished in different ways. For example:

- Immersion cooling: all the parts of the motor, included windings and bearings, are completely submerged in cryogenic liquid (see Figure 1.3).
- Forced-flow cooling: in this method the cooling liquid circulates just through the windings that are made of hollow conductors [4].
- External cooling: this method consists in cooling only the outside of the motor directly or indirectly with a cryogenic fluid.
- Contact cooling: it involves direct contact with a cooling medium, enabling efficient heat transfer.

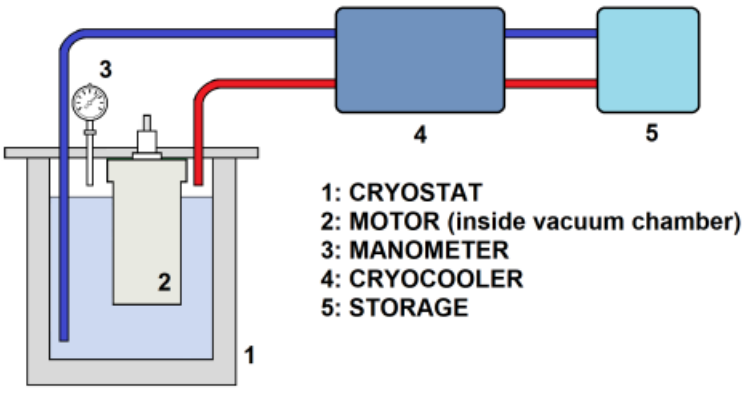


Figure 1.3: Typical submerged cooling system of an electric motor

### 1.1.2 Advantages of Cryogenic Operations

Compared with room temperature operations, thanks to the decrease of the electric resistivity (and joule losses consequently) and the superior heat extraction capability of the fluid, cryogenic conditions allow higher power and torque density, increased load capability, increased power factor and increased efficiency [3, 5]. In addition, due to the cryogenic coolant, there are less thermal limitations for the whole stable zone of the torque-speed characteristics [6]. In [7] an increase in output power between +96% and +189% and an increase in efficiency between +30% and +35 % were observed, while in [6] an increase in torque of 171 % was observed.

### 1.1.3 Disadvantages of Cryogenic Operations

Cryogenic cooling requires a complex cryostat for its implementation that may not justify, in terms of complexity and costs, the increase of the electrical machine efficiency and loading capability [6]. Safety issues have to be taken into account as well.
From the technical point of view, core losses are generally higher with respect to those of air-cooled machines since the electrical conductivity of laminations increases at lower temperature [8]. Furthermore, the presence of the fluid in the airgap causes a remarkable increase in friction losses compared to an air-cooled machine [5].
Additionally, given that the rotor resistance is lower compared to ambient conditions and considering the starting torque is directly proportional to this resistance, the starting torque is subsequently reduced. This could pose an issue for loads with significant inertia at zero speed, as they demand a high starting torque.
Lastly, given that the current industry predominantly relies on conventional motors, integrating cryogenic motors with existing industrial systems may pose challenges.

To sum up, in Table 1.1 are listed the main advantages and disadvantages of cryogenic motors with respect to the conventional ones.

| Advantages | Disadvantages |
|---|---|
| Lower resistance and joule losses | Complexity of the cooling |
| Higher power and torque density | Lower starting torque |
| Higher efficiency | Higher iron losses |
| Higher heat extraction capability | Higher mechanical losses |
| Higher load capability | Costs |
| Higher power factor | Integration with existing systems |

Table 1.1: Advantages and disadvantages of cryogenic machines with respect to conventional ones

## 1.2 Superconducting Electric Machines

Superconductors are materials that can carry electrical current with zero resistance, typically at very low temperatures. The operation of the machine at cryogenic temperatures also allows investigating the use of these materials, in the form of bulks (Figure 1.4) and tapes (Figure 1.5), in place of conventional conducting materials in the fabrication of windings, permanent magnets and flux shields to obtain superior performance.

Figure 1.4: Different shapes of HTS bulk superconductors

In Figure 1.5, it is noteworthy that the superconducting component is the ReBCO (Rare-element, Barium, and Copper) layer. With a thickness of only $1\mu m$, it can handle a current density of approximately $10^6 A/cm^2$ [9]. The remaining layers are primarily for barrier and support purposes.

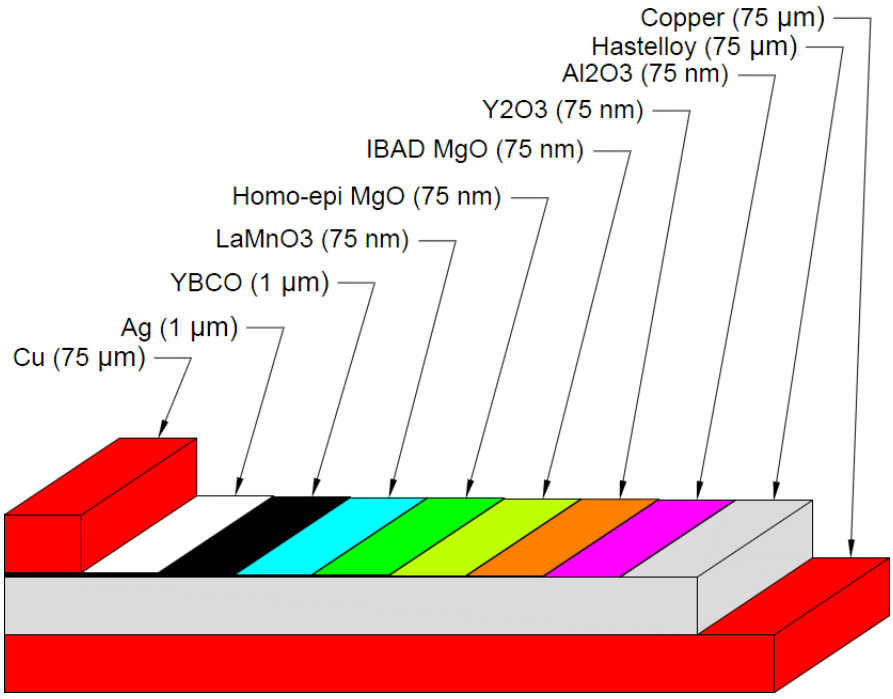


Figure 1.5: Second Generation (2G) HTS YBCO tape superconductor

Currently, two kinds of superconductors are available in the market: the low-temperature superconductors (LTS) and the high-temperature superconductors (HTS). The main difference, besides the composition, regards the working temperature range since the LTS are superconducting below 30K while HTS between 77K and 120K.

The refrigeration complexities and costs of LTS have been an issue for their widespread into the electric machine market. Starting with an empirical breakthrough in 1989, however, a strong set of large scale demonstration devices have been made with high temperature superconductors. Given their significantly larger thermal margin and their ability to facilitate simpler cooling systems, HTS are better suited for the implementation of superconducting machines.[10–12].
To summarize the difference in performance between a conventional machine, a cryogenic machine with conventional materials and a cryogenic machine with superconductors, the Table 1.2 has been created, where one star '*' indicates the worst machine and three stars '***' indicate the best machine.

| | Conventional Machine | Cryogenic Machine | Superconducting Machine |
|---|---|---|---|
| Current Density | * | ** | *** |
| Output Power | * | ** | *** |
| Output Torque | * | ** | *** |
| Efficiency | * | ** | *** |

Table 1.2: Performance comparison between conventional and cryogenic machines

## 1.3 Early Applications

The earliest applications of cryogenic motors were driven predominantly by necessity. Electric motors, particularly pumps, were required to function in environments involving liquids and gases at extremely low temperatures. For instance, pumps used in space exploration or medical applications might need to handle cryogenic substances like liquid oxygen or liquid nitrogen.
As countries rebuilt their economies following WWII, the demand for natural gas increased throughout the world. Much of this imported gas had to come from overseas fields and to transport economically, gas was liquefied at the production sites and transported by ship to the receiving nations. The first submerged cryogenic motors were used to move this liquefied gas from shore to ship and, subsequently, from ship back to shore. These first motors were immersed in liquid methane at -161 °C[11]. Figure 1.6 shows instead a modern application of a cryogenic pump for liquified natural gas.

Figure 1.6: Cryogenic submerged pumps for liquified natural gas (LNG) by Vanzetti Engineering

One of the compelling reasons for designing such motors was to eliminate the need for thermal barriers [13]. By submerging the motor directly into the cold liquid, the necessity for intricate isolation methods between the motor and the cryogenic medium could be bypassed. Figure 1.7 shows the section of a submerged pump for liquified natural gas applications.

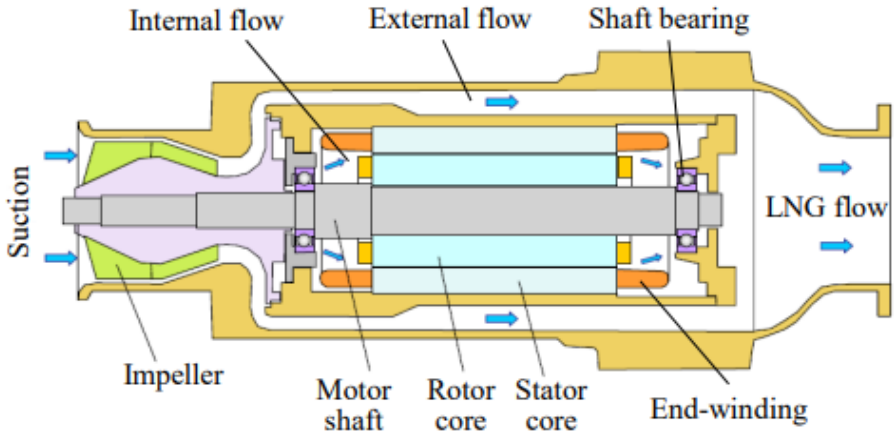


Figure 1.7: Submerged pump assembly for LNG applications using a cryogenic-cooled induction machine

Moreover, many of the problems associated with ambient temperature motors, such as partial discharge, corona, thermal life, and oxidation, were absent on submerged motor[11]. During the design phase, however, it is necessary to take into account the characteristics (electrical, mechanical and thermal) of materials at low temperatures and the differences with respect to room temperature operations. In fact, while cryogenic conditions allow a higher efficiency and torque, it makes no sense to operate a conventional motor at cryogenic

temperature to obtain the same rated power. In other words, to achieve the best efficiency at the desired torque, the machine design must be optimized for cryogenic conditions.[14–16]

## 1.4 Future Trends

Over time, the emphasis on using cryogenic motors shifted. Instead of being used only for applications that inherently demanded operation at low temperatures, cryogenic cooling started to be employed to enhance energy efficiency. Using cryogenic fluids exclusively for cooling purposes can significantly boost the performance of a motor.

### 1.4.1 Electrification of Aircraft

The aeronautics industry is anticipating deep changes and new challenges in the near future. It is expected that air traffic will continue to grow in the next decades even taking into account the impact of COVID-19, social acceptability and long-term roadmaps such as ACARE (Advisory Council for Aeronautics Research in Europe) Flightpath 2050. The SRIA (Strategic Research and Innovation Agenda) set specific goals such as a 75% reduction of CO2 emissions and 90% reduction of Nitrogen Oxides (NOx) as a result of ecological and sustainable development obligations. With this in mind, the aerospace industry has initiated a technological transition toward electrification with the so-called More Electric Aircraft (MEA). This more-electric design has been proven to reduce the fuel consumption of the aircraft by replacing mechanical, pneumatic, and hydraulic energy sources with electric energy. The MEA concept became a commercial reality in 2005 with the Airbus A380, followed by the Boeing 787 (Figure 1.8).

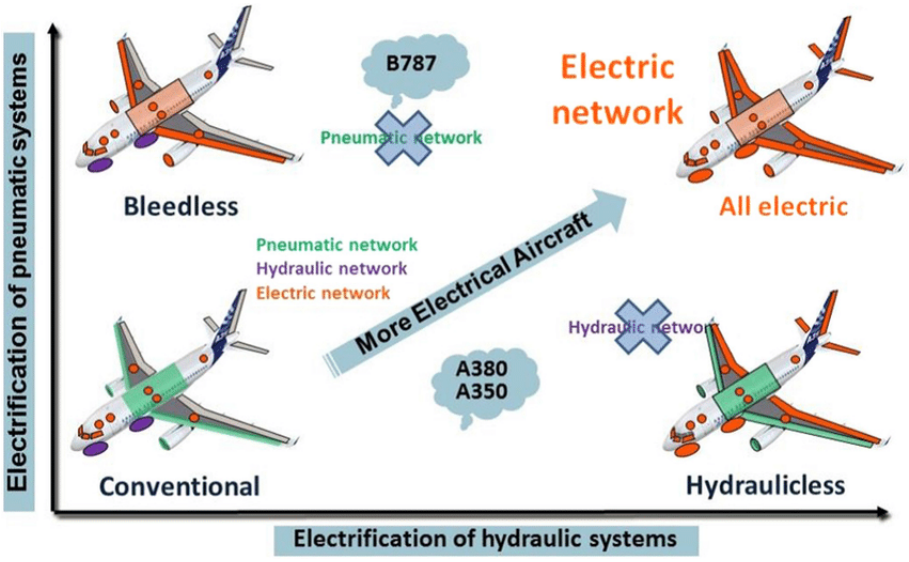


Figure 1.8: Aircrafts evolution: from conventional to more electric

Traditional MEA, however, still uses fossil fuel for propulsion, which requires 90% of total energy consumption. To further reduce emissions, a high efficient, high specific power electrical propulsion system is urgently needed: the goal is to achieve a specific power greater than 10 kW/kg [17–20].
A promising avenue to replace conventional fuel, thanks to its high specific energy, is liquid hydrogen; whether to burn it in a turbofan or to use it in a fuel cell to generate electrical power. A lot of work is currently underway on fuel cell or H2-burn propulsion but it remains essential to develop an ultra-efficient electric or hybrid propulsion system for the future aircraft. If a cryogenic source like liquid hydrogen is available on board, it can be used in two ways to increase performance of electric machines, as has been already specified in Section 1.2: using conventional cryogenic motors or superconducting motors [21].

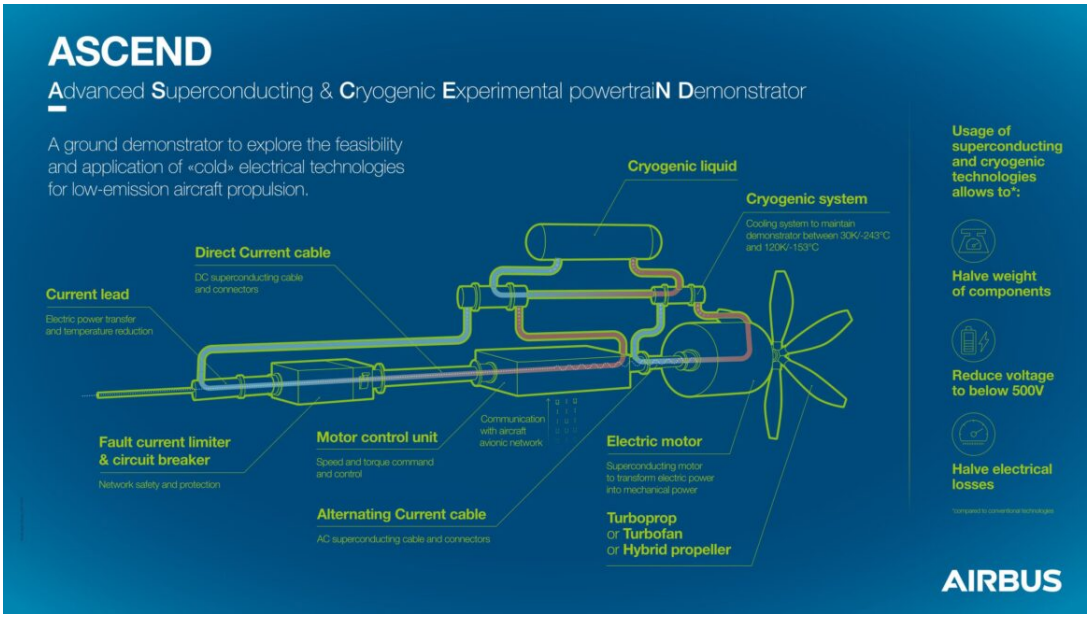


Figure 1.9: ASCEND (Advanced Superconducting and Cryogenic Experimental powertraiN Demonstrator)

Airbus has recently launched the "Advanced Superconducting and Cryogenic Experimental powertraiN Demonstrator" (see Figure 1.9) to explore the impact of superconducting materials and cryogenic temperatures on the performance of an aircraft's electrical propulsion systems.

### 1.4.2 Naval Propulsion

After an increasing demand for large ships for goods transportation, the cruise industry prompted tremendous research and development. Those efforts resulted in the development of today's small all-electric ships and large hybrid vessels that provide more fuel efficiency and less air pollution. The main drivers behind the movement toward electric ships include the International Maritime Organization (IMO) and rising fuel prices. To minimize the air

pollution caused by the container ships that transport goods across the globe, the IMO adopted stringent regulations limiting nitrogen oxide (NOx) and sulfur oxide (SOx) emissions [22].
Electric propulsion was seldom used until the 1980s, when the development of power electronics technologies enabled the efficient variable-speed control of electric motors. One of the main benefits of electric propulsion is the ability to maintain high efficiency across a wide operational speed. Variable speed controlled electric motors have a high efficiency (around 95%) between 5% and 100% of rated power, while for combustion engine the optimum efficiency is just in the small range 85%–90% of rated power [23].
Here are listed the main types of ship propulsion systems:

- Diesel Electric: diesel engines are coupled with generators, whose generated electricity powers an electric motor. Diesel engines can operate at an optimal regime to produce electricity, regardless of the ship's speed, thus increasing the efficiency of the system.
- Turbo-Electric Drive: turbo-electric propulsion is commonly adopted in fast ferryboat applications and modern cruise ships. In this case, diesel engines are replaced by one or more gas turbines. Gas turbines offer a reduced volume and produce fewer emissions.
- Hybrid Diesel–Turbo-Electric: this is a mixed layout, which includes a diesel engine and a gas turbine (see Figure 1.10).

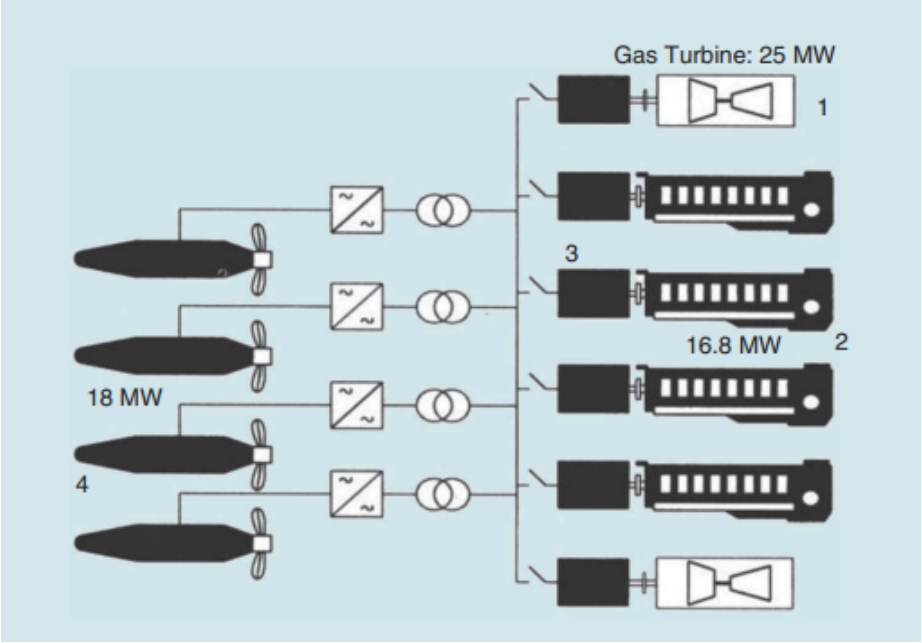


Figure 1.10: An example of Hybrid Diesel–Turbo-Electric configuration

Since the importance of electric motors in naval propulsion, the use of high efficiency cryogenic superconducting motors has been investigated these years. In [24], for example, a lightweight, compact, high efficiency, high power superconducting LTS motor for ship propulsion

has been designed.
In [25], an induction motor operating on a U.S. Navy warship rated 5000 hp, 590 V, 60 Hz, and 1791 r/min has been investigated for comparing both conventional and emerging technologies. HTS motors 2G technology have been found to be the best solution for high-power applications where size and weight are the main considerations, such as the high-power dense propulsion motors. The results can be seen in Table 1.3.

| | Induction Motor | PM Motor | HTS Motor |
|---|---|---|---|
| Volume $[m^3]$ | 0.80 | 0.56 | 0.41 |
| Torque density $[kNm/m^3]$ | 26 | 42 | 53 |
| Efficiency | 96.37% | 97.62% | 98.72% |

Table 1.3: Performance comparison between conventional and cryogenic motors for naval propulsion

## 1.5 Goal of the Thesis

This thesis project has been carried out in Lisboa, at Instituto Superior Técnico and more precisely in the Laboratório de Máquinas Elétricas (LME).

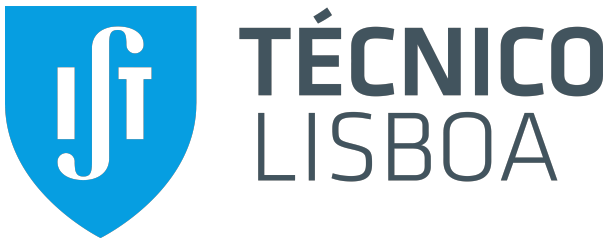


Figure 1.11: Instituto Superior Técnico Lisboa

Although a general introduction was made also on superconducting machines, this thesis focuses on cryogenic machines with conventional materials. In particular the object of our study is a 90W induction motor with liquid nitrogen cooling.
The motor underwent standard laboratory testing (no-load, locked rotor, and load tests) both at room temperature and under cryogenic conditions to determine the equivalent circuit parameters and conduct power, torque and efficiency studies.
The primary goal is therefore to compare its performance in these two different working conditions. Moreover, a comparative analysis will be conducted with a similar 90W induction motor that was previously tested.

# Chapter 2

# Ambient Tests

## 2.1 Standard Tests on Induction Motors

This section outlines the Standard Tests for induction motors, useful to determine the equivalent circuit parameters as well as the performance and the efficiency. The approach follows the guidelines provided in the "IEEE Standard Test Procedure for Polyphase Induction Motors and Generators"[26].

### 2.1.1 Winding Resistance

The winding resistance measurement is the first test to be performed. With the machine at ambient temperature, the terminal-to-terminal winding resistance has to be measured with the machine connected in the configuration to be used in the efficiency testing. All the combination between the three phases must be measured to assure that the specific precise value needed in further analyses will be available.
It is also important to measure and record the ambient temperature.

### 2.1.2 No-load Test

This test is performed by running the machine as a motor at rated voltage and frequency with no connected load. When separation of no-load losses is to be accomplished, it is suggested to record three or more values of voltages between 125% and 75% of the nominal voltage, with a point near 100% rated voltage, and three or more values of voltage between 50% and 20% of rated voltage. It is also possible to see an increase in current while reducing the voltage: in this case the test has to be stopped. The measured input power is the total of the losses in the motor at no load. These losses consist of the stator, $P_{js}$, friction and windage, $P_{fw}$, and core losses, $P_{core}$.

$$P_{in} = P_{js} + P_{fw} + P_{core} \tag{2.1}$$

Since the input power is measured and the stator losses can be computed knowing the value

of the stator resistance, only $P_{fw}$ and $P_{core}$ have to be determined.
To determine the friction and windage loss, the stator losses must be subtracted from the input power and the resulting power curve must be plotted against voltage. The intercept with the zero voltage axis represents the friction and windage loss.
The core losses can be finally determined as the difference between the input power and the other losses.

### 2.1.3 Locked Rotor Test

For this test it is necessary to lock the rotor shaft and supply the machine with a reduced voltage. Simultaneous readings of voltage and current in all phases and of power input at several levels of voltage must be recorded, with special care in the neighborhood of full-load current. Taking the highest readings first and the lower readings in succession will help to equalize the temperature.
It is important, to avoid injuries, to identify the direction of the rotation before starting the test, especially for high torque motors. It has also to be noticed that the testing of induction machines under locked rotor conditions involves high mechanical stresses and high rates of heating.
Moreover, the rotor of a squirrel-cage motor is a symmetrical bar winding; therefore, the impedance of the motor is practically the same for any position of the rotor relative to the stator. The impedance of a wound-rotor motor, however, varies with the position of the rotor relative to the stator. It is therefore necessary when performing a locked-rotor impedance test to determine the rotor position that results in an average value of impedance.

### 2.1.4 Load Test

The load test is essential to determine the performance and the efficiency. The machine is coupled to a load machine and is subjected to loads at four load points approximately equally spaced between not less than 25% and up to and including 100% load, and two load points suitably chosen above 100% load, but not exceeding 150% load. More than six load points may be used if desired.
In loading the machine, it is suggested to start at the highest load value and move in descending order to the lowest.

## 2.2 Induction Motor Electromechanical Model

The three-phase induction motor is commonly analyzed using its single-phase equivalent circuit. This approach is valid only when the three phases are perfectly balanced and symmetrical. The equivalent circuit is very useful to compute the torque, the power, the efficiency and all the others electromechanical characteristics.
Figure 2.1 shows the steady state single phase equivalent circuit of an induction motor. All the parameters of the rotor are referred to the stator side.

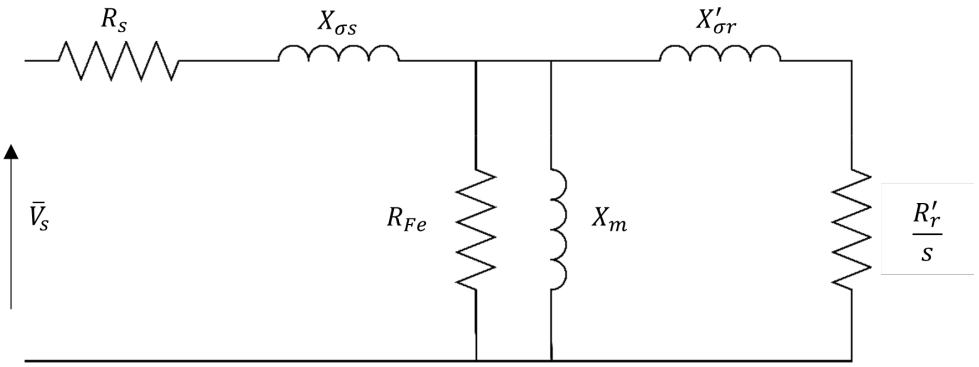


Figure 2.1: Single phase equivalent circuit of an induction motor

Where:

- $R_s$ represents the resistance of the stator windings;
- $X_{\sigma s}$ represents the leakage reactance of the stator winding;
- $R_{Fe}$ represents the iron losses due to eddy currents and hysteresis;
- $X_m$ is the magnetizing reactance associated with the magnetizing current that creates the rotating magnetic field;
- $X'_{\sigma r}$ represents the leakage reactance of the rotor squirrel cage;
- $\frac{R'_r}{s}$ can be seen as the sum of $R'_r$ and $R'_r \cdot \frac{1-s}{s}$. The former represents the real resistance of the squirrel cage while the latter is a fictitious resistance that represents the electromechanical conversion.

## 2.3 Motor Under Test and Measurement Devices

The motor under test is a small 90 W three phase induction motor. The following Table 2.1 shows the nameplate data.

| | | |
|---|---|---|
| Nominal power | 90 | W |
| Nominal phase-to-phase voltage | 40 | V |
| Nominal current | 4.1 | A |
| Nominal speed | 1370 | rpm |
| Nominal Torque | 0.627 | Nm |
| Nominal power factor | 0.80 | |
| Nominal efficiency | 39.6% | |
| Number of pole pairs | 2 | |
| Insulation class | F | |

Table 2.1: Motor under test nameplate

Figure 2.2 is a picture of the motor under test.

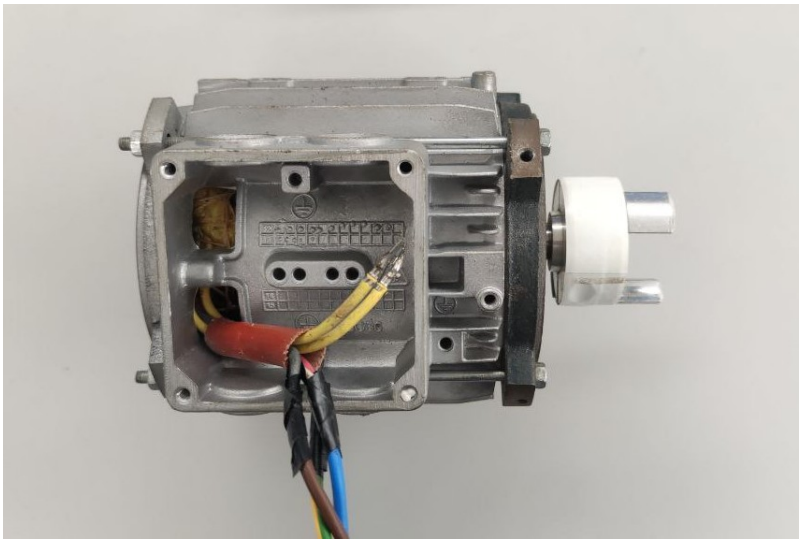

Figure 2.2: Picture of the induction motor under test

The measurement system is equipped with three voltage and three current sensors that provide instantaneous waveform data. This data is captured using a National Instruments device, specifically the NI USB-6009. Once acquired, the data is analyzed in MATLAB, enabling the calculation of various parameters such as the RMS values of current and voltage, active, reactive, apparent power and power factor.

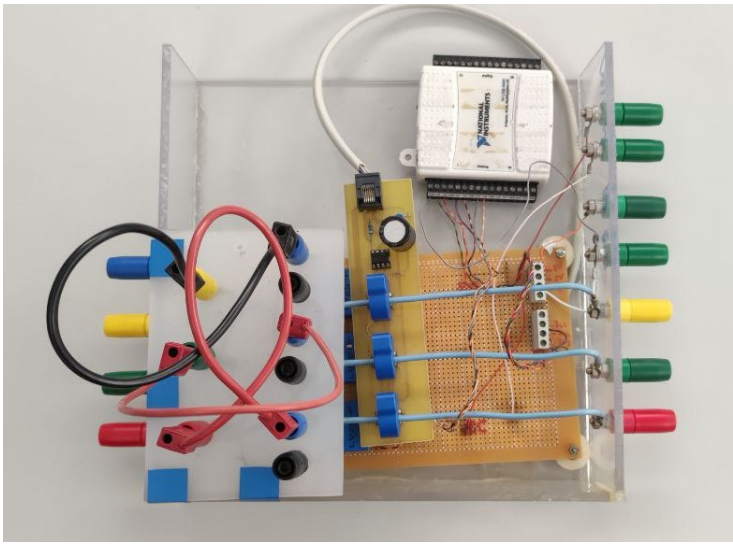

Figure 2.3: NI measurement device and conditioning circuit

Other external measurement devices have been used:

- A multimeter to check the phase voltage to remain in the operating range;
- A current clamp to check the phase current to remain in the operating range;
- An optical speed sensor to measure the rotor speed.

## 2.4 No-load Ambient Test

With the no-load test, it is possible to determine the transverse parameters of the equivalent circuit $R_{Fe}$ and $X_m$. Powering the motor at grid frequency, the voltage is increased to reach the nominal voltage and then it is reduced in several steps to reach about the 30% of the nominal voltage.
Firstly, the stator resistance value is required. It can be determined through a DC measurement by powering two phases of the motor, as illustrated in Figure 2.4.

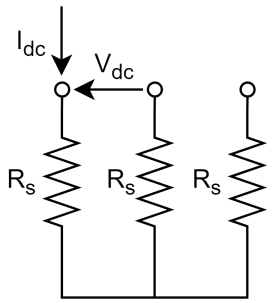


Figure 2.4: Electrical schematic for the measurement of the stator resistance

$$V_{dc} = 2R_s I_{dc} \rightarrow R_s = 0.5 \cdot \frac{V_{dc}}{I_{dc}} \tag{2.2}$$

This procedure is repeated three times for every possible phase to check that the resistances have the same values.
Then, for each voltage step, the following procedure has been carried on:

- Measuring the input power $P_{in}$, voltage $V_{Ph-N}$ and current $I_s$ through the NI device
- Computing the joule losses as $P_{Cu} = 3 \cdot R_s \cdot I_s^2$
- Computing iron plus mechanical losses as $P_{Fe} + P_{mech} = P_{in} - P_{Cu}$

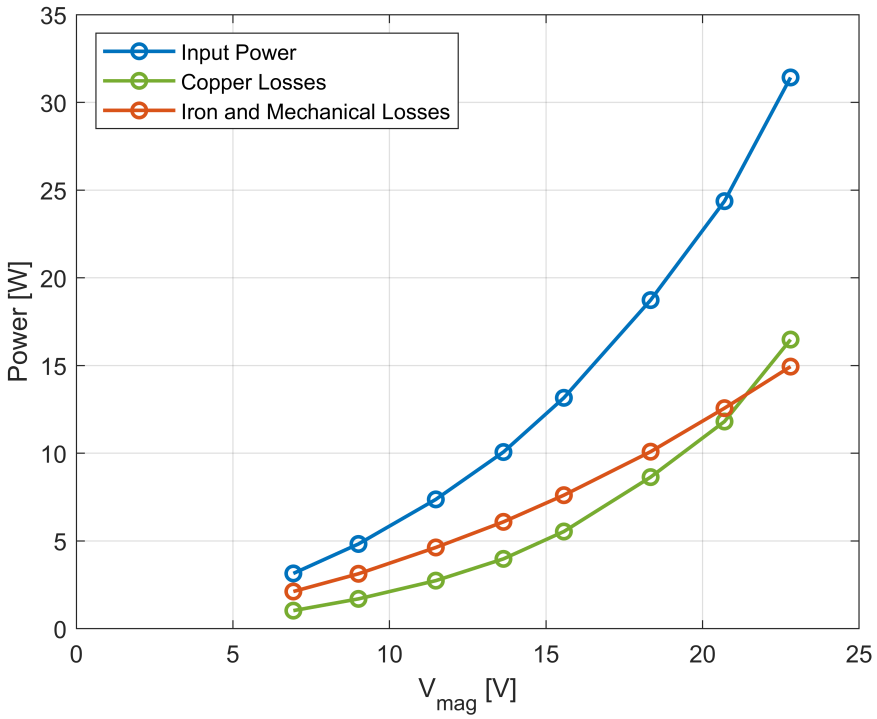


Figure 2.5: No-load ambient test: input power, copper losses, mechanical and iron losses

Iron losses are composed of hysteresis losses ($\propto B^2 f$) and eddy currents losses ($\propto B^2 f^2$). Since the frequency remains constant during the test, iron losses are proportional to $B^2$ and consequently to $(V/f)^2$. The mechanical losses are proportional to the square of the rotor speed, but in the no load test the speed remains almost constant and so they can be considered constant.
When the voltage goes to zero, the iron losses would also go to zero, and thus, only mechanical losses would remain. However, without voltage the machine would also stop. Therefore, a quadratic fit is used on the mechanical and iron losses to estimate the mechanical losses from its interception with the y-axis (see Figure 2.6).

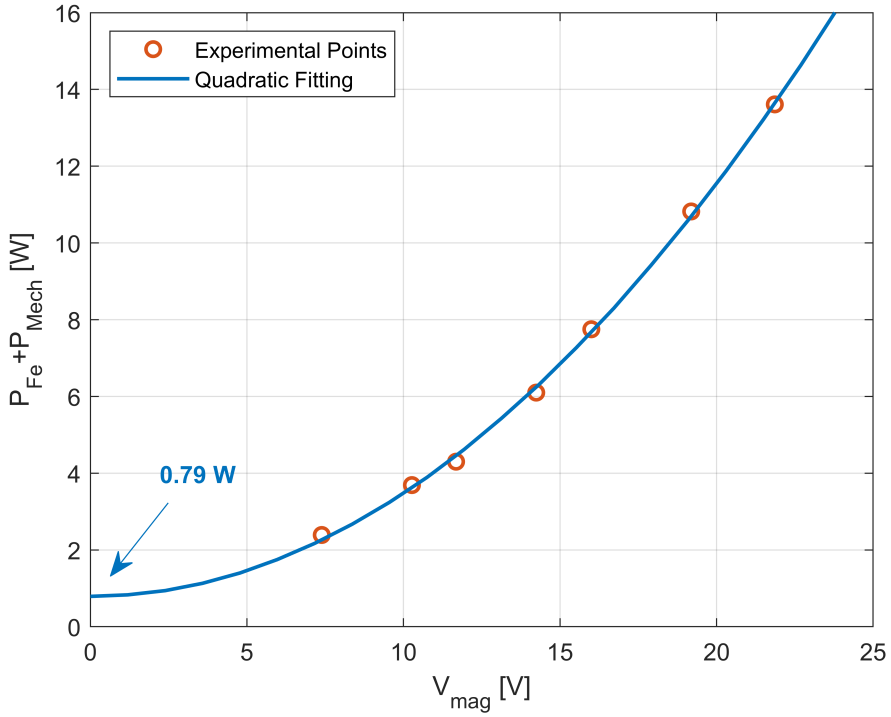


Figure 2.6: No-load ambient test: mechanical and iron losses as a function of the magnetizing voltage

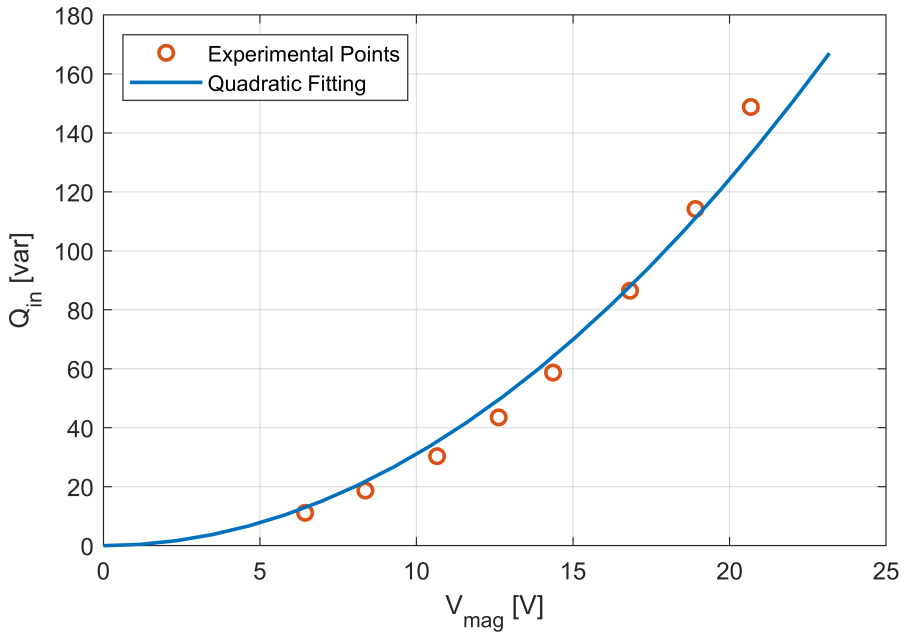


Figure 2.7: No-load ambient test: reactive power as a function of the magnetizing voltage

To determine the parameters, we can consider the equivalent circuit in Figure 2.1. Being at

no load means that the secondary is an open circuit. We can write the following formulas:

$$P_{Fe} = 3 \cdot \frac{V_{mag}^2}{R_{Fe}} \tag{2.3}$$

$$Q_{in} = 3 \cdot \frac{V_{mag}^2}{X_m} \tag{2.4}$$

Where $V_{mag}$ is the magnetizing voltage applied to the transverse impedance, considering the voltage drop on the stator resistance and neglecting the stator leakage reactance.

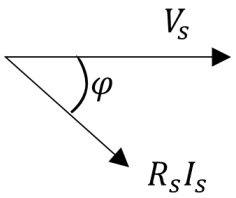


Figure 2.8: Phasor diagram illustrating the stator voltage and current

Looking at the phasor diagram in Figure 2.8, the formula is the following:

$$V_{mag} = \sqrt{(V_s - R_s I_s cos\varphi)^2 + (R_s I_s sin\varphi)} \tag{2.5}$$

By performing a polynomial fitting of the Figures 2.6 and 2.7, it is possible to obtain the equivalent circuit parameters (Table 2.2) using the following equations:

$$P_{Fe} + P_{Mech} = A + B \cdot V_{mag}^2 \rightarrow \begin{cases} R_{Fe} = \dfrac{3}{B} \\ P_{Mech} = A \end{cases} \tag{2.6}$$

$$Q_{in} = C \cdot V_{mag}^2 \rightarrow X_m = \frac{3}{C} \tag{2.7}$$

| | | |
|---|---|---|
| $R_{Fe}$ | 111.11 | Ω |
| $X_m$ | 11.21 | Ω |
| $P_{Mech}$ | 0.79 | W |

Table 2.2: Parameters obtained from the no-load test

## 2.5 Locked Rotor Ambient Test

The locked rotor test has the purpose to determine the longitudinal parameters $R'_r$, $X_{\sigma s}$, $X'_{\sigma r}$.
In a dual way with respect to the no load test, the motor is powered at grid frequency and the current is increased to reach the nominal current; then it is reduced in several steps up to zero.
Since the voltage is much smaller than the nominal one and the reactance $X_m$ is bigger than the longitudinal impedance, we can neglect the transverse parameters $R_{Fe}$ and $X_m$ responsible respectively for the iron losses and the magnetizing current.
For each step it is possible to measure the input power $P_{in}$ and consequently to compute the apparent power and the reactive power with the following formulas:

$$S_{in} = V_{s1} \cdot I_{s1} + V_{s2} \cdot I_{s2} + V_{s3} \cdot I_{s3} \tag{2.8}$$

$$Q_{in} = \sqrt{S_{in}^2 - P_{in}^2} \tag{2.9}$$

where $V_{si}$ and $I_{si}$ are the RMS values of each phase.
Moreover, we know that:

$$P_{in} = 3 \cdot (R_s + R'_r) \cdot I_s^2 \tag{2.10}$$

$$Q_{in} = 3 \cdot (X_{\sigma s} + X'_{\sigma r}) \cdot I_s^2 \tag{2.11}$$

Plotting the graphs of the active and reactive power versus the current and performing a polynomial fit, it is possible to obtain the desired values, assuming $X_{\sigma s}$ and $X'_{\sigma r}$ to be equal.

$$P_{in} = A \cdot I_s^2 \;\rightarrow R'_r = \frac{A}{3} - R_s \tag{2.12}$$

$$Q_{in} = B \cdot I_s^2 \;\rightarrow X_{\sigma s} + X'_{\sigma r} = \frac{B}{3} \;\rightarrow X_{\sigma s} = X'_{\sigma r} = \frac{B}{6} \tag{2.13}$$

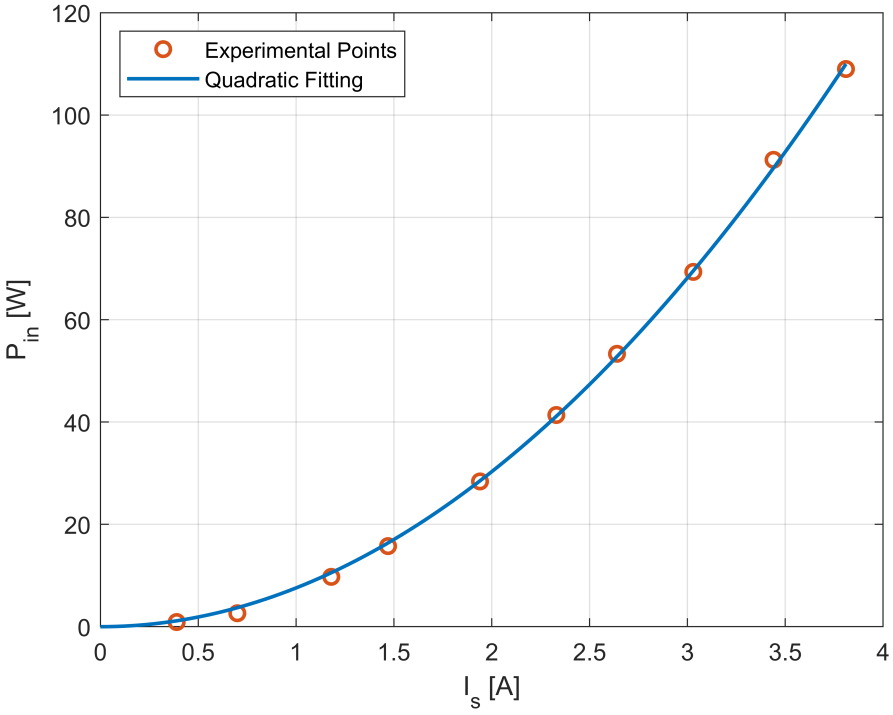


Figure 2.9: Locked rotor ambient test: input active power as a function of the stator current

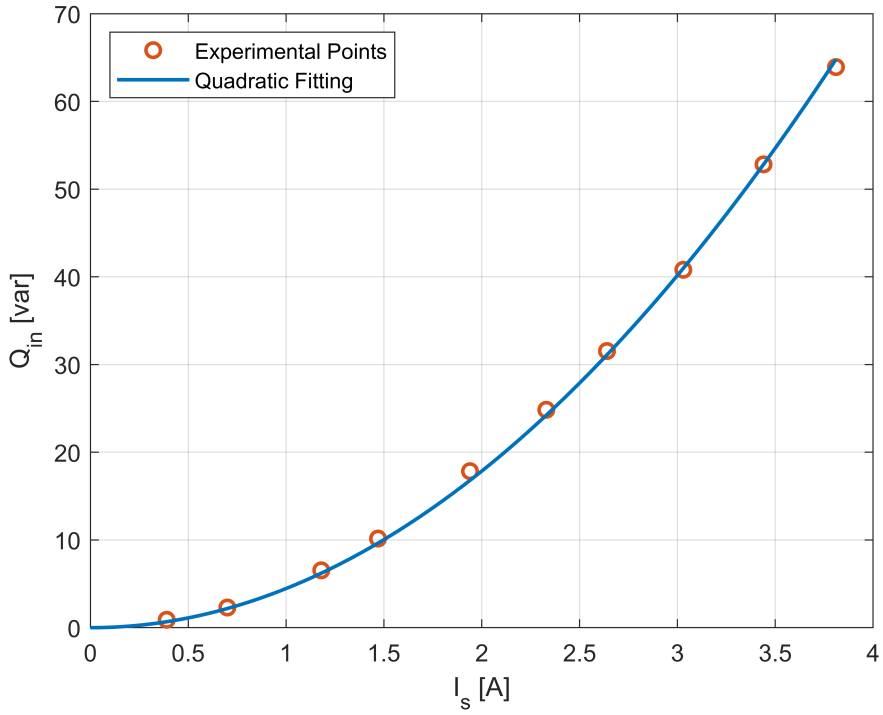


Figure 2.10: Locked rotor ambient test: input reactive power as a function of the stator current

It is important to note that the stator resistance value used in Equation 2.12 was measured

after the locked rotor test. Due to the resulting temperature increase, this value is higher. By measuring this resistance, the temperature variation can also be estimated.
It is well known the following relation between the resistivity of a material and the temperature:

$$\frac{\rho_2}{\rho_1} = \frac{|\theta_c| + \theta_2}{|\theta_c| + \theta_1} \tag{2.14}$$

Where $\theta_c$ is the crtical temperature of the material. In case of the copper, $\theta_c = -234.5°C$ (Figure 2.11).
According to the First Ohm's Law, since the geometry of the conductors does not change, it is possible to write the Equation 2.14 in terms of resistance:

$$\frac{R_2}{R_1} = \frac{|\theta_c| + \theta_2}{|\theta_c| + \theta_1} \tag{2.15}$$

Where the values $R_1 = 1.15\ \Omega$ and $R_2 = 1.20\ \Omega$ are respectively the stator resistance before and after the test. We can apply Equation 2.16, to find the increase in temperature from the beginning to the end of the test.

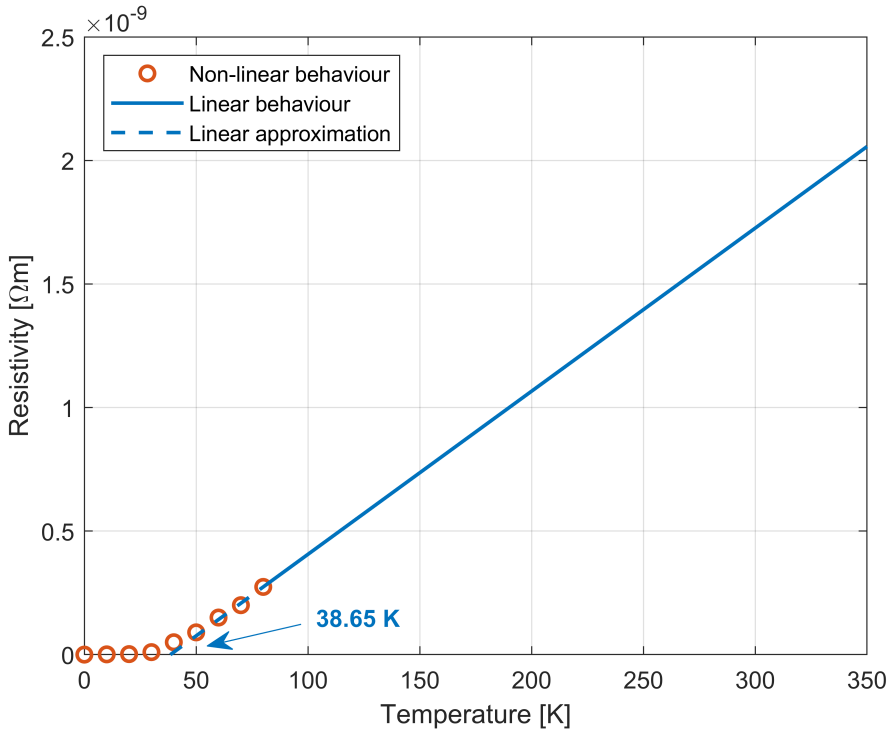


Figure 2.11: Electric resistivity of copper as function of the temperature

Figure 2.11 depicts the true resistivity curve for the copper. Even though its behavior is not linear at low temperatures (as indicated by the red dots), our work, in this initial phase, is conducted at room temperature, making the linear approximation suitable. The critical temperature was identified by tracing the dashed blue line and marking its intersection with

the temperature axis, resulting in $\theta_c = -234.5°C$. Finally, since our focus is only on the temperature difference, we set $\theta_1 = 0°C$.

$$\theta_2 = \frac{R_2}{R_1} \cdot (|\theta_c| - \theta_1) - |\theta_c| = 10.2°C \tag{2.16}$$

We can therefore estimate an increase in temperature of 10.2 degrees from the beginning to the end of the test. To summarize:

| | Before test | After test |
|---|---|---|
| Stator resistance | 1.15 Ω | 1.20 Ω |
| Temperature | 25°C | 35.2°C |

Table 2.3: Stator resistance and temperature before and after the locked rotor test

In conclusion, the values of the longitudinal parameters are the following:

| | |
|---|---|
| $R_s$ | 1.150 Ω |
| $R'_r$ | 1.316 Ω |
| $X_{\sigma s}$ | 0.827 Ω |
| $X'_{\sigma r}$ | 0.827 Ω |

Table 2.4: Parameters obtained from the locked rotor test

## 2.6 Load Ambient Test

When testing a motor, one of the essential parameters to measure is the torque. In scenarios where a direct torque sensor is not available, an alternative method is to use a DC generator (with separate excitation in this case) coupled to the motor. The DC generator effectively serves as a torque transducer. By measuring the armature current of the generator, we indirectly obtain information about the torque the motor is producing.

### 2.6.1 DC Machine Characterization

The equations of a DC machine, working as a motor, are the following:

$$V_a = R_a \cdot I_a + L_a \cdot \frac{dI_a}{dt} + E_a \tag{2.17}$$

$$E_a = k_\Phi(I_f) \cdot \omega_r \tag{2.18}$$

$$T = k_\Phi(I_f) \cdot I_a \tag{2.19}$$

In Equation 2.17, since we are studying the steady state, the voltage drop on the inductance is zero.

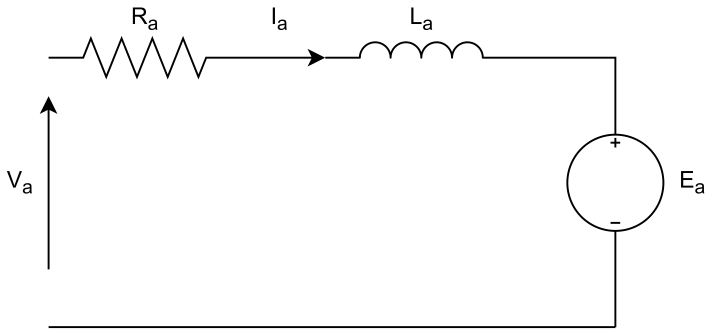


Figure 2.12: DC Machine equivalent circuit

The purpose of the test is to determine the armature constant $k_\Phi$ as a function of the field current and to determine copper losses, iron losses and mechanical losses.
The machine has been run as a motor and the following quantities have been measured: $V_a$,$I_a$,$R_a$,$V_f$,$I_f$,$\omega_R$, where $V_f$ and $I_f$ are the excitation voltage and current.
By keeping the field current constant at its nominal value, different armature voltage have been applied; then the field current has been decreased in discrete steps and, for each value, the armature voltage has been changed as before.

Starting from Equations 2.17 and 2.18, the armature constant has been computed, in each step, as:

$$k_\Phi = \frac{V_a - R_a \cdot I_a}{\omega_R} \tag{2.20}$$

Later, the following plot has been made:

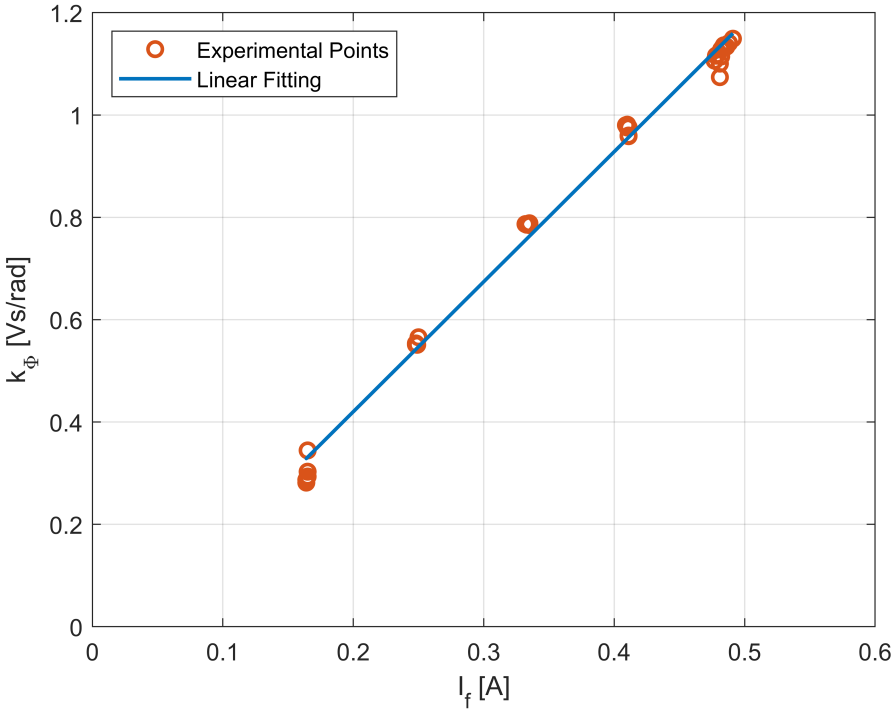


Figure 2.13: Armature constant of the DC Machine

Regarding the losses, copper losses have been computed as:

$$P_{Cu} = R_a \cdot I_a^2 \tag{2.21}$$

Going on, it is possible to obtain the iron and mechanical losses:

$$P_{Fe} + P_{mech} = P_{in} - P_{Cu} \tag{2.22}$$

A 3D map has been created in order to determine these losses by knowing the excitation current and the rotor speed as input.

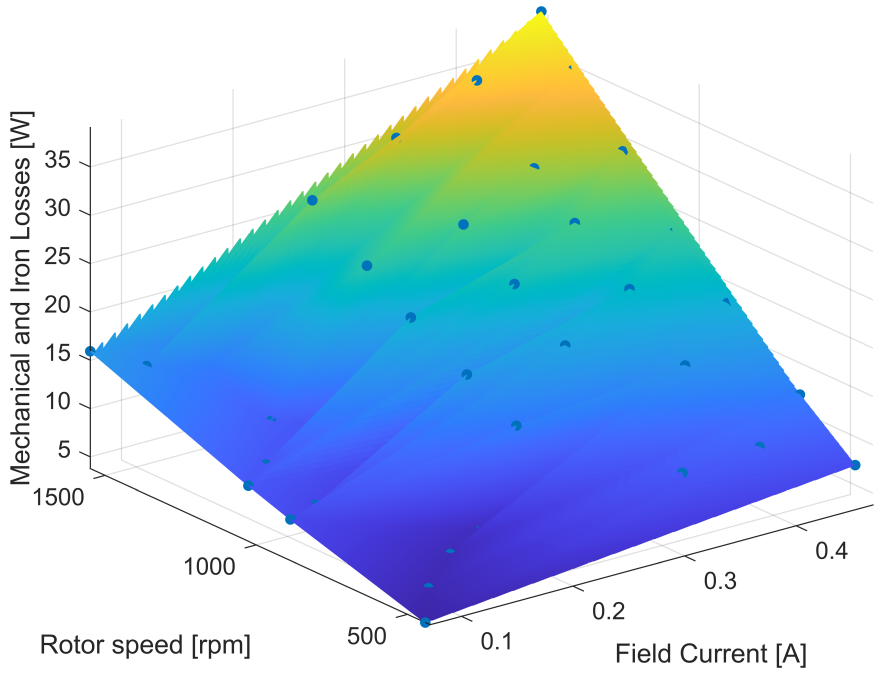


Figure 2.14: Mechanical and iron losses map as function of the rotor speed and field current

### 2.6.2 Experimental Setup

As said before, the induction motor under test is coupled with a DC machine that serves as a load and works as a generator. In particular the armature circuit is connected with a fixed resistance and the excitation circuit is connected with a DC source. By varying the excitation current it is possible to change the load: the higher the current, the higher the torque and vice versa. The induction motor is powered at nominal voltage and nominal frequency. The excitation current is first set in order to have the nominal current in the induction motor, then it is decreased in several steps to decrease the load.
The electrical schematic is the following:

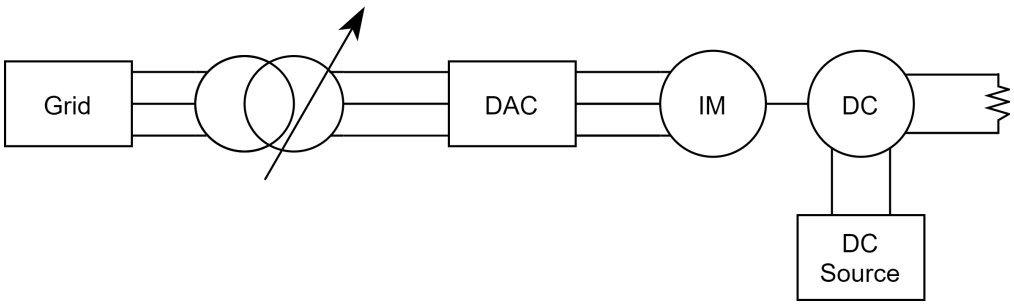


Figure 2.15: Load test electrical schematic

The real implementation is represented in Figure 2.16.

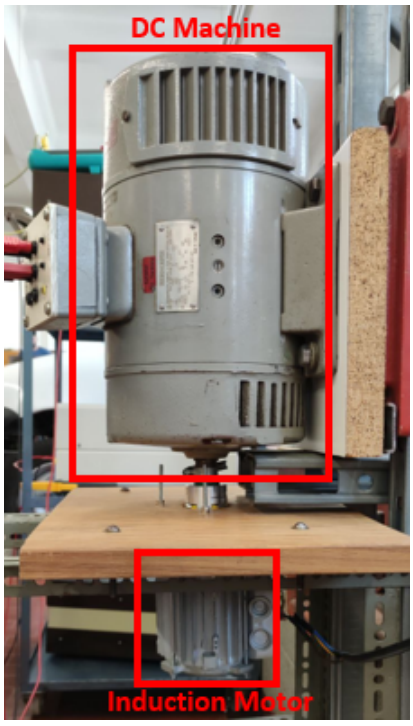


Figure 2.16: Ambient load test experimental setup

The main purpose of the load test is to determine the output torque and efficiency of the induction motor. The power chain is presented in the following diagram.

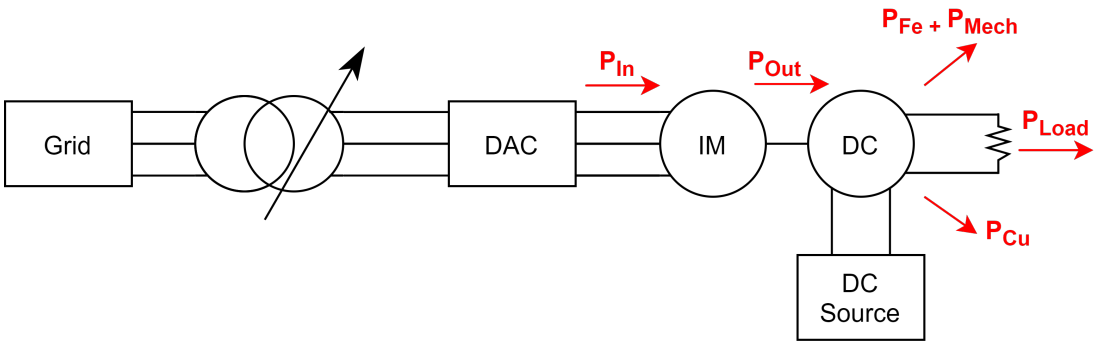


Figure 2.17: Load test power chain

It is possible to compute the output power of the induction motor as:

$$P_{out} = P_{Cu} + (P_{Fe} + P_{Mech}) + P_{Load} \tag{2.23}$$

Where:

- $P_{Cu} = R_a \cdot I_a^2$, where both the quantities are measured
- $P_{Fe} + P_{Mech}$ can be determined knowing the field current (measured) and the rotor speed (measured) through the map in Figure 2.14

- $P_{Load} = V_a \cdot I_a$, where both the quantities are measured

Measuring the input power and knowing the output power it is possible to compute the torque and the efficiency respectively as:

$$T = \frac{P_{out}}{\omega_r} \tag{2.24}$$

$$\eta = \frac{P_{out}}{P_{in}} \tag{2.25}$$

### 2.6.3 Theoretical Analysis

Since all the parameters of the equivalent circuit have been determined (Table 2.2 and Table 2.4), it is possible to compute analytically the quantities under investigation in order to compare them with the experimental points. The only input data needed for the theoretical analysis is the phase voltage $V_s$
Starting from the circuit in Figure 2.1 it is possible to simplify it using network theorems as follows.

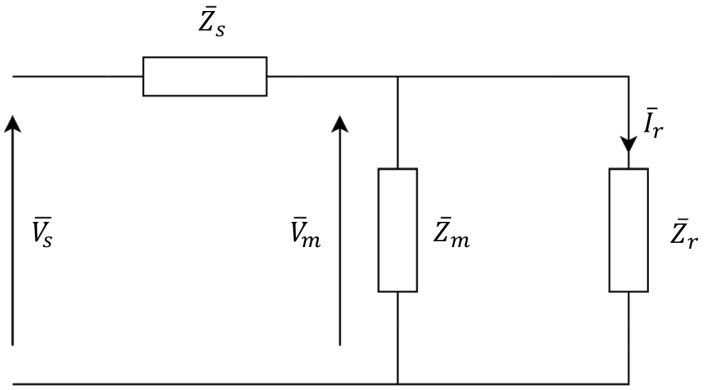


Figure 2.18: Single phase equivalent circuit simplification step 1

Where:

- $\overline{Z}_s = R_s + jX_{\sigma s}$ is the stator impedance
- $\overline{Z}_m = \dfrac{R_{Fe} \cdot jX_m}{R_{Fe} + jX_m}$ is the magnetizing impedance
- $\overline{Z}_r = \dfrac{R'_r}{s} + jX'_{\sigma r}$ is the rotor impedance

Now we can make the parallel between the two branch, obtaining thus the following circuit:

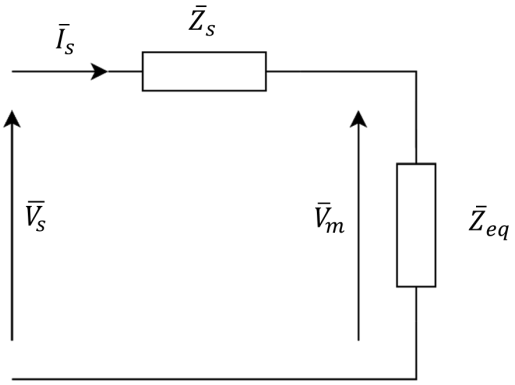


Figure 2.19: Single phase equivalent circuit simplification step 2

Where:

$$\overline{Z}_{eq} = \frac{\overline{Z}_m \cdot \overline{Z}_r}{\overline{Z}_m + \overline{Z}_r} = R_{eq} + jX_{eq} \tag{2.26}$$

$$\overline{V}_m = \overline{V}_s - \overline{Z}_s \cdot \overline{I}_s \tag{2.27}$$

$$\overline{I}_r = \frac{\overline{V}_m}{\overline{Z}_r} \tag{2.28}$$

Now it is possible to compute analytically the torque having as input only the parameters of the equivalent circuit, the number of pole pairs (p) and the electrical frequency ($\omega = 2\pi f$)

$$T = 3 \cdot \frac{p}{\omega} \cdot \frac{R'_r}{s} \cdot I_r^2 \tag{2.29}$$

It is now possible to compute the output power simply as:

$$P_{out} = T \cdot N_r \cdot \frac{\pi}{30} \tag{2.30}$$

Where $N_r$ is the rotational speed of the rotor in rpm.
Considering the equivalent circuit of Figure 2.19, we can compute the input power of the motor as:

$$P_{in} = 3 \cdot V_s \cdot I_s \cdot cos\varphi \tag{2.31}$$

Where:

$$I_s = \frac{V_s}{\sqrt{(R_{eq} + R_s)^2 + (X_{eq} + X_{\sigma s})^2}} \tag{2.32}$$

$$\varphi = arctan\left(\frac{X_{eq} + X_{\sigma s}}{R_{eq} + R_s}\right) \tag{2.33}$$

Hence, the efficiency is:

$$\eta = \frac{P_{out}}{P_{in}} \tag{2.34}$$

### 2.6.4 Results

Now that all the parameters have been computed and all the data acquired, it is possible to compare the analytical curve with the experimental points.
Two different plots will be analyzed:

- Speed vs Torque
- Speed vs Efficiency

#### Speed vs Torque Characteristics

To perform a correct analysis of the data it is important to point out that the analytical curve, described in Equation 2.29, depends on the voltage as can be seen in Figure 2.20.

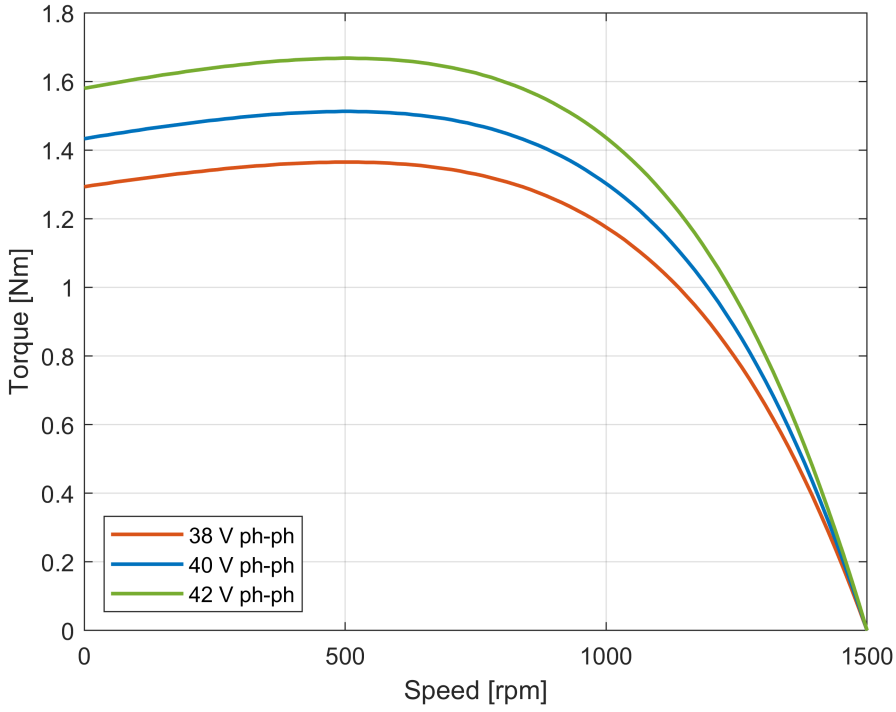


Figure 2.20: Speed vs torque characteristic as function of the voltage

Therefore, when comparing the experimental points with the analytical curve, it is necessary to draw the curve using the same average voltage used to perform the load test.

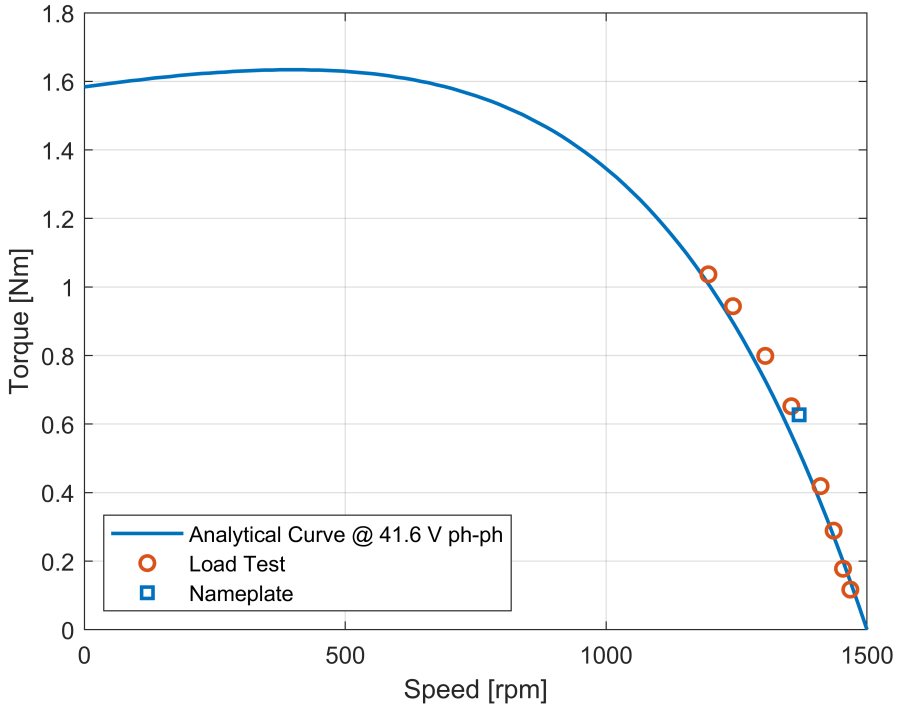


Figure 2.21: Speed vs torque ambient characteristics - analytical curve and experimental points

It is possible to see that the analytical curve fits quite well the experimental points of the load test.
The small difference could be explained through some reasonings about the rotor resistance $R'_r$, that is responsible for the slope of the linear working zone in the torque speed graph: the lower the resistance, the higher the slope and vice versa.
It is known that the locked rotor test is the worst for the increase of the temperature in the rotor because the slip is equal to 1 and the induced currents at stator frequency cause high iron losses. Now, since the analytical curve is plotted based on the no-load and locked rotor test, it is possible that the rotor resistance is higher, with respect to the real one in the load test, because the temperature in the locked rotor test is higher.
The goal is to find which is the difference of temperature between the locked rotor and load test that permits the two curves, analytical and experimental, in Figure 2.21 to be perfectly overlapped.

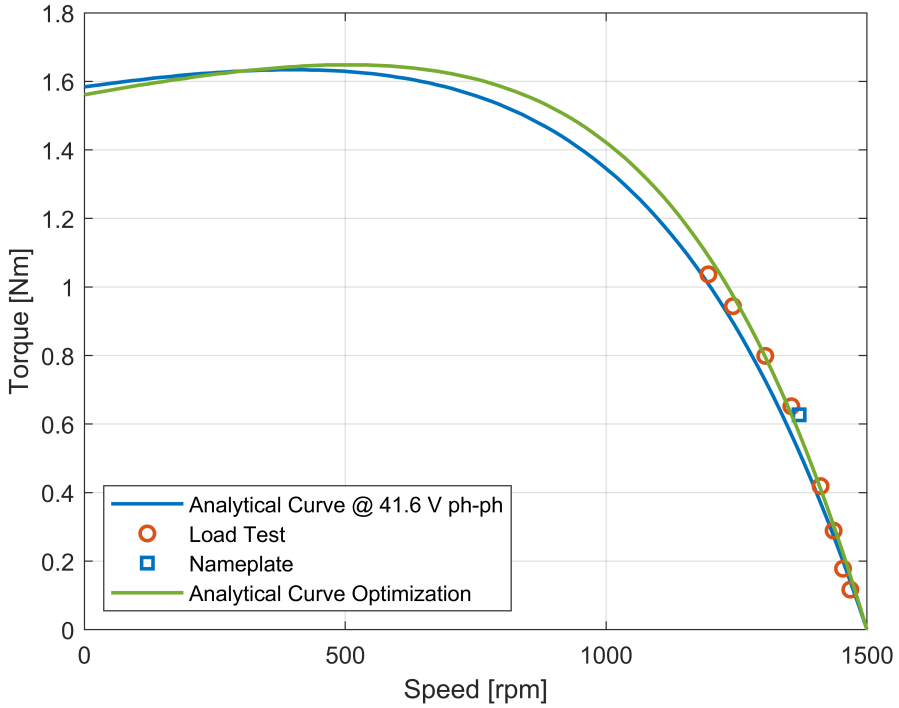


Figure 2.22: Speed vs torque ambient characteristics - analytical curve and experimental points optimization

Through an optimization process, many values of $R'_r$ have been tested in the range $1.1 \div 1.3\ \Omega$ since the optimum resistance should be lower than $1.316\ \Omega$ as can be seen in Table 2.4.
The parameter to evaluate the optimum fit is the coefficient of determination $R^2$:

$$R^2 = 1 - \frac{SSR}{SST} \tag{2.35}$$

Where SSR is the Sum of Squared Residuals and SST is the Total Sum of Squares. Let (x,y) represent the observed values (experimental curve) and $(x; \hat{y})$ the predicted values obtained by evaluating the same input x using the analytical expression. The formulas are the following:

$$SSR = \sum_{i=1}^{n} (y_i - \hat{y}_i)^2 \tag{2.36}$$

$$SST = \sum_{i=1}^{n} (y_i - \bar{y})^2 \tag{2.37}$$

Where $\bar{y}$ represents the average of the observed values.
In Table 2.5 is represented the optimum value for $R'_r$ and the correspondent coefficient of determination.

| $R'_{r,opt}$ | $R^2$ |
|---|---|
| 1.24 Ω | 0.9929 |

Table 2.5: Results of the optimization process for the speed vs torque ambient characteristics

With the values $R_1 = 1.316\ \Omega$ and $R_2 = 1.24\ \Omega$ determined, we can apply Equation 2.38 to find the optimal temperature reduction from the locked rotor to the load test for the best data fit. Here again, as in Section 2.5, even though the behavior of aluminum is not linear at low temperatures, the linear approximation for temperatures higher than 100K can be used. The critical temperature can be seen in Figure 2.23 and corresponds to $\theta_c = -265.65°C$. Finally, we set $\theta_1 = 0°C$ for simplicity.

$$\theta_2 = \frac{R_2}{R_1} \cdot (|\theta_c| - \theta_1) - |\theta_c| = -15.3°C \tag{2.38}$$

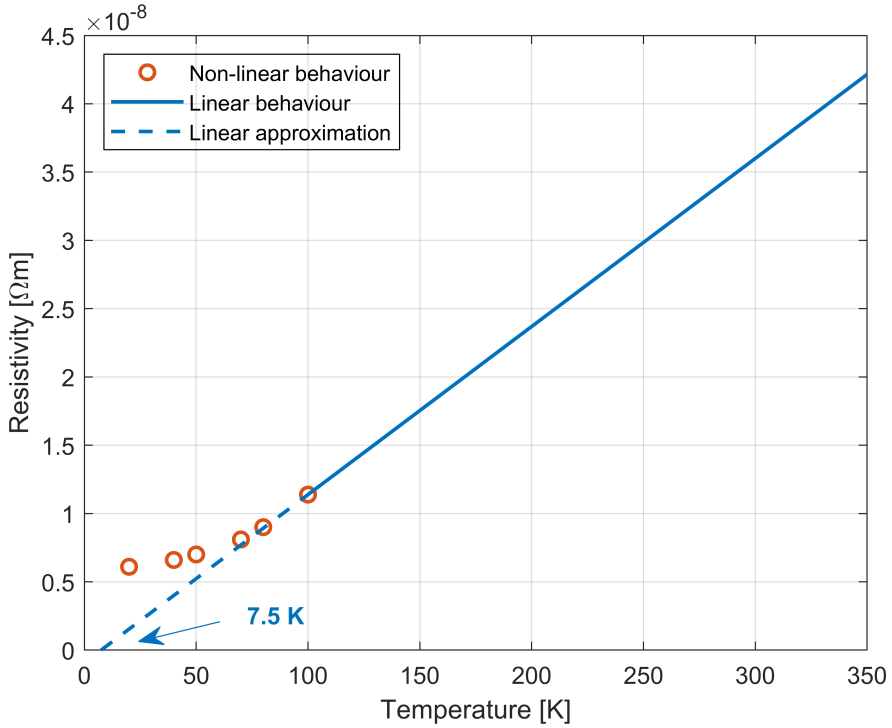


Figure 2.23: Electric resistivity of the aluminum alloy 2024-0 as function of the temperature

In the end, for the most accurate fit of the data, we need to assume that the rotor temperature during the load test is 15.3 degrees lower than the one of the locked rotor test.

### Speed vs Efficiency Characteristics

Regarding the efficiency, in Figure 2.24, again the analytical curve and the experimental points are almost overlapped. However, the nominal efficiency written in the nameplate seems to be not close neither to the analytical curve nor to the experimental curve.

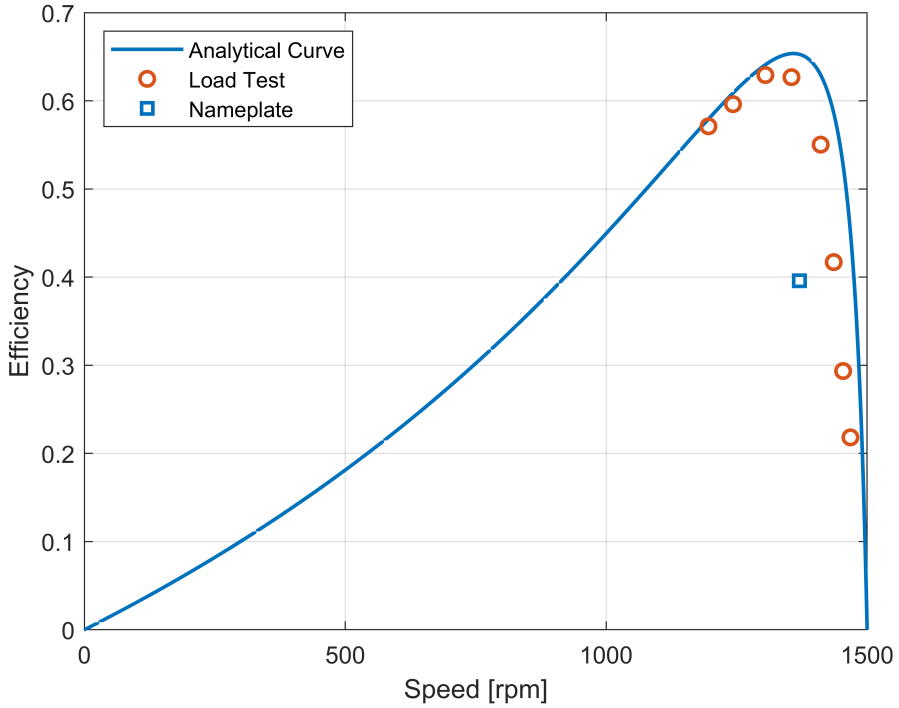


Figure 2.24: Speed vs efficiency ambient characteristics - analytical curve and experimental points

The small difference between the analytical curve and the experimental points can be improved looking at the following circuit.

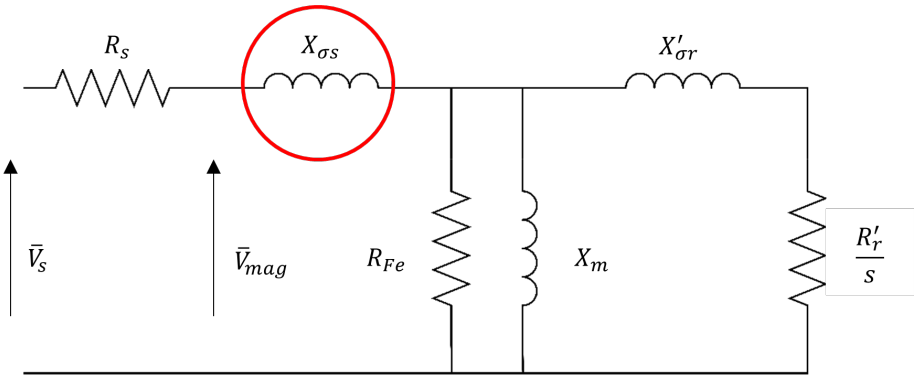


Figure 2.25: Equivalent circuit of induction motor highlighting the presence of the stator leakage reactance

As shown in Formula 2.5 in the load test procedure, regarding the magnetizing voltage, only the effect of the stator resistance has been considered. This can be seen in Figure 2.25. However, if we also consider the effect of the stator leakage reactance, we can say that the magnetizing voltage is applied to both $X_{\sigma s}$ and $X_m$. Therefore we can create a new plot, the green curve in Figure 2.26, subtracting $X_{\sigma s}$ from the value of $X_m$.

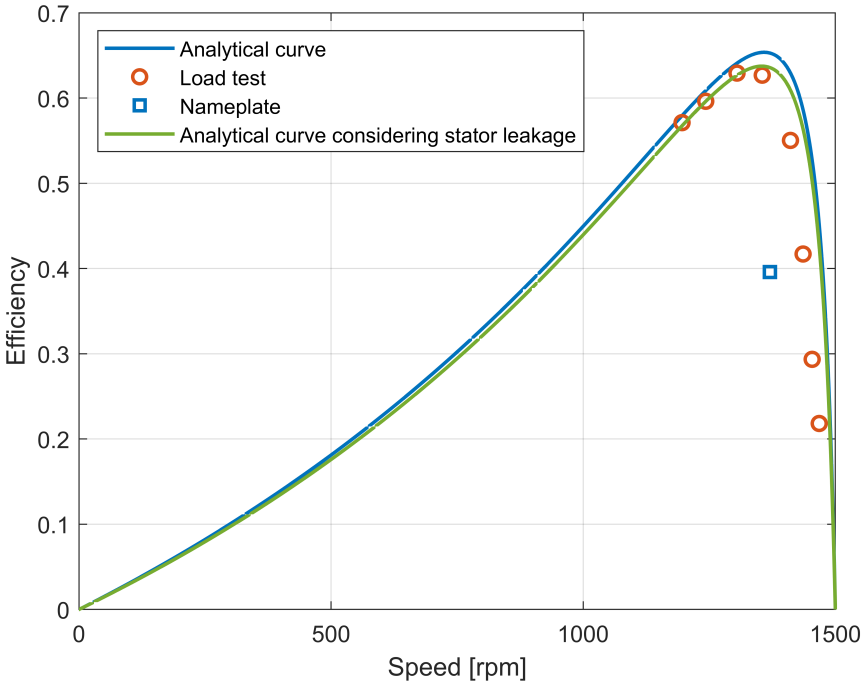


Figure 2.26: Speed vs efficiency characteristics considering stator leakage reactance

Having a lower magnetizing reactance means having a higher magnetizing current, thus reducing the efficiency (see Figure 2.27). That is why the green curve is lower than the blue curve and fits better the experimental points.

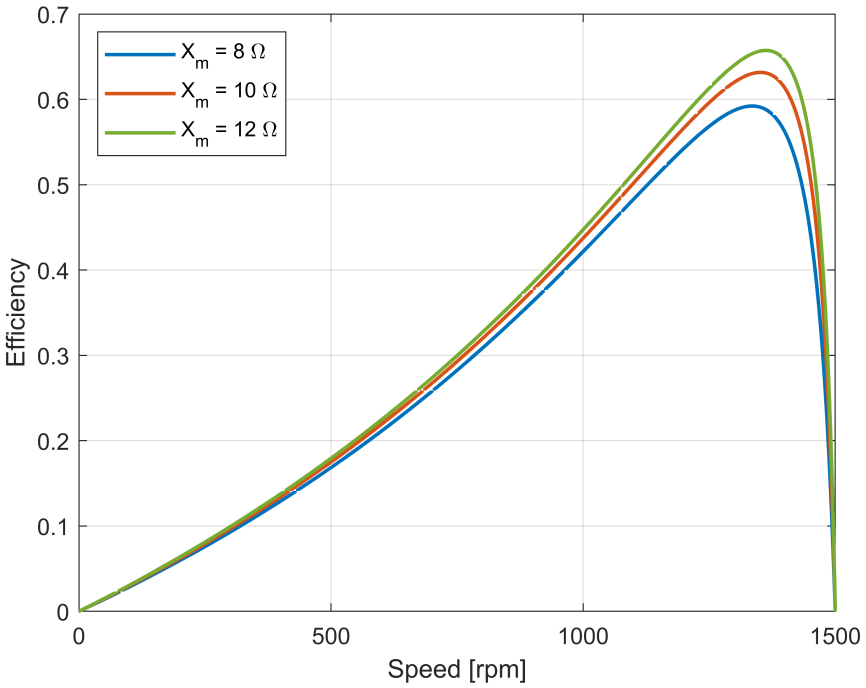


Figure 2.27: Speed vs efficiency characteristics as function of the magnetizing reactance

## 2.7 Comparison with a Similar Motor

The motor under test (MUT) has been called Motor II. The reason is that, previously, a similar motor (Motor I) had been tested. In Table 2.6 it is possible to see the differences between the two nameplates and in Figure 2.28 it is possible to see a picture of the two motors.

| | Motor I | | Motor II (MUT) | |
|---|---|---|---|---|
| Rated voltage (ph-ph): | 40 | V | 40 | V |
| Rated current: | 3.6 | A | 4.1 | A |
| Rated frequency: | 50 | Hz | 50 | Hz |
| Rated power: | 0.09 | kW | 0.09 | kW |
| Pole pairs: | 2 | | 2 | |
| Rated speed: | 1350 | rpm | 1370 | rpm |
| Rated torque: | 0.637 | Nm | 0.627 | Nm |
| Rated power factor: | 0.610 | | 0.800 | |
| Rated efficiency: | 59.2% | | 39.6% | |

Table 2.6: Nameplates comparison between Motor I and Motor II (MUT)

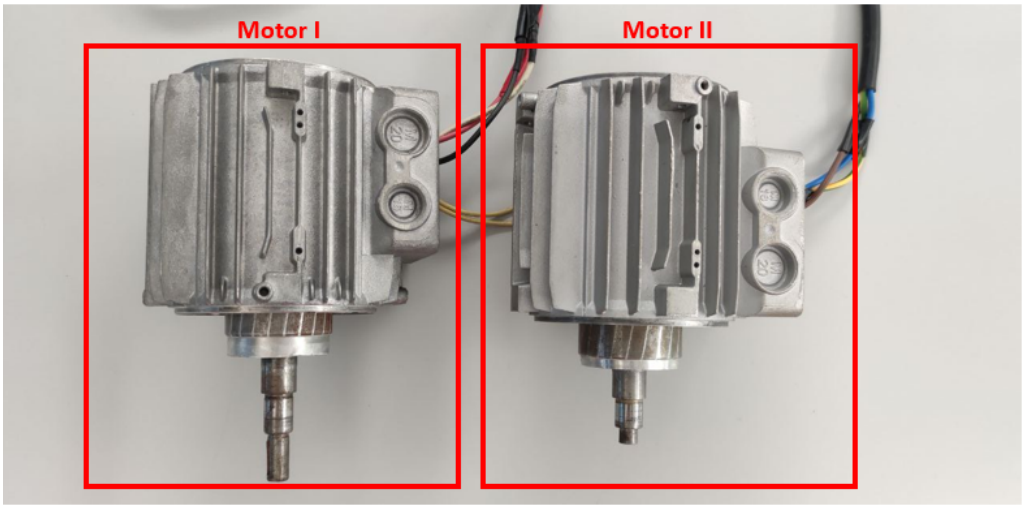


Figure 2.28: Comparison of the dimensions of the two 90W induction motors

### 2.7.1 No-load and Locked Rotor Test Comparison

For Motor I, as well as for Motor II, no-load and locked rotor tests had been carried on in order to determine the equivalent circuit parameters. The results are reported in Table 2.7.

| | Motor I | | Motor II (MUT) | |
|---|---|---|---|---|
| Equivalent iron losses resistance | 116.4 | Ω | 111.11 | Ω |
| Equivalent magnetizing reactance | 7.33 | Ω | 11.21 | Ω |
| Stator resistance | 1.10 | Ω | 1.15 | Ω |
| Rotor resistance | 0.914 | Ω | 1.316 | Ω |
| Stator reactance | 0.532 | Ω | 0.827 | Ω |
| Rotor reactance | 0.532 | Ω | 0.827 | Ω |

Table 2.7: Equivalent circuit parameters comparison between Motor I and Motor II (MUT) at ambient conditions

The iron losses resistance and the stator resistance are very similar for both motors. The biggest differences regards the magnetizing reactance, the rotor resistance and the leakage reactances.
In motor II, due to the smaller air gap, the magnetizing reactance is higher. As a result, less magnetizing current is required for a given voltage to establish the magnetic flux and magnetize the core.
Regarding the rotor resistance, motor II contains less aluminum in the rotor bars, thus increasing the resistance.
The difference between the leakage reactances depends on the different geometry of the slots.

### 2.7.2 Load Test Comparison

#### Speed vs Torque Characteristics

In Figure 2.29 the speed vs torque characteristics of the two motors can be seen. The differences between them can be explained looking at the equivalent circuit parameters in Table 2.7. In particular:

- The slope of the linear working region is lower for Motor II since its rotor resistance is higher
- The peak of the curve is lower for Motor II since the stator and rotor reactance are higher.

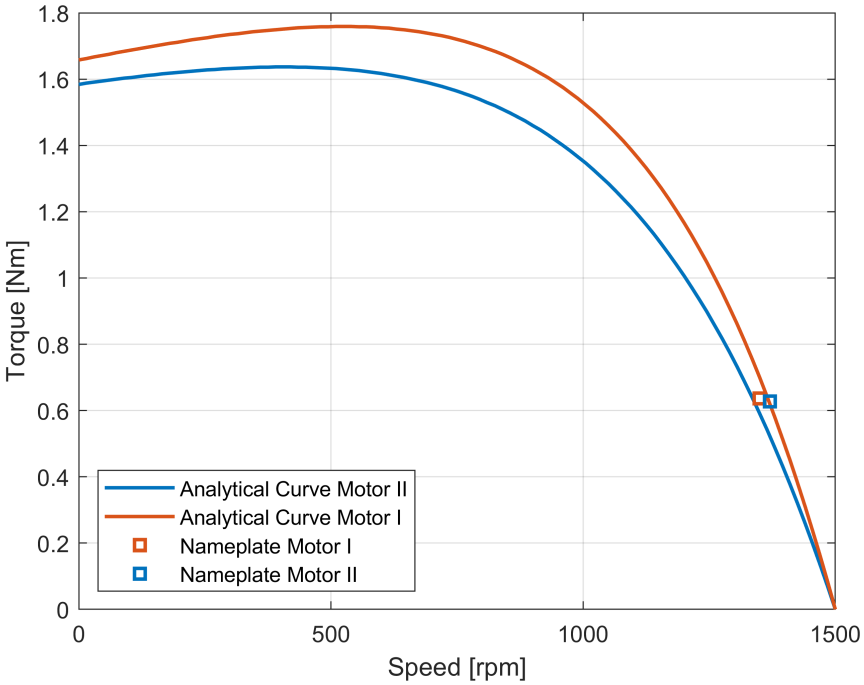


Figure 2.29: Speed vs torque ambient characteristics comparison between Motor I and Motor II (MUT)

In Figure 2.30 the load tests data have been added. For both motors, the results are similar and they match the respective analytical curves.

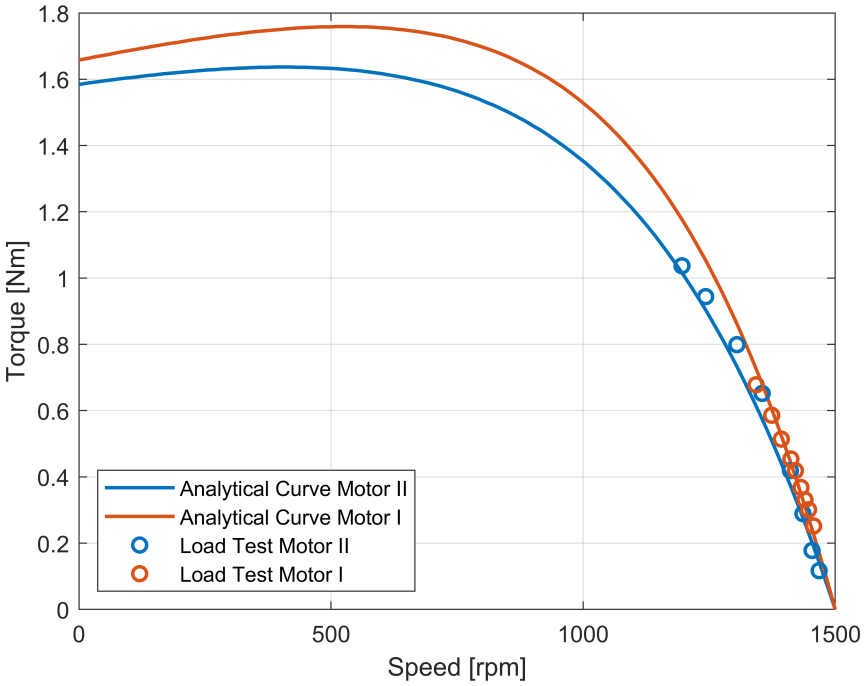


Figure 2.30: Speed vs torque ambient characteristics and load test comparison between Motor I and Motor II (MUT)

### Speed vs Efficiency Characteristics

Before commenting the results, a brief summary of how the parameters of the equivalent circuit influence the efficiency must be done.

- The equivalent iron losses resistance is responsible for the iron losses. If the resistance is higher, the iron losses are lower and in the end the efficiency is higher.
- The equivalent magnetizing reactance is related with the magnetizing current. This is the current absorbed from the motor in order to create the rotating magnetic field and it does not produce torque.
  In the end, if the reactance is higher, the magnetizing current is lower and so the efficiency is higher, as already shown in Figure 2.27.
- The stator and rotor resistance are responsible for the joule losses. Therefore having higher resistances means higher losses and lower efficiency.
- The stator and rotor reactances, being longitudinal parameters, have a dual effect with respect to the magnetizing reactance that is a transverse parameter. Having higher stator and rotor reactance means having higher reactive current and therefore lower efficiency.

In Figure 2.31 both the analytical curves and the results of the load tests have been reported.

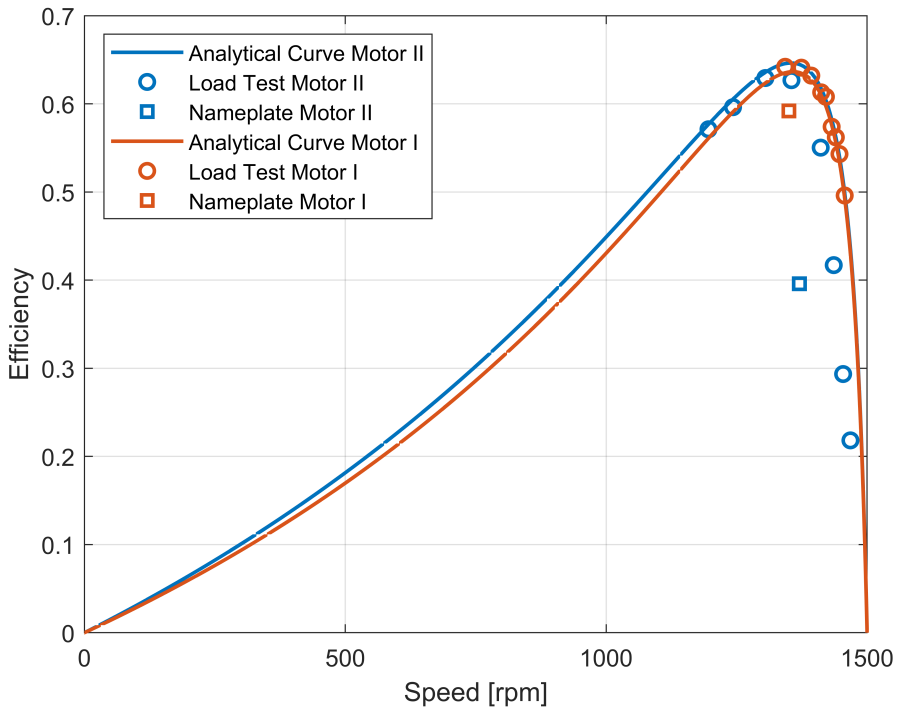


Figure 2.31: Speed vs efficiency characteristics comparison

As we can see, both the analytical curves and the experimental points of the two motors are very similar. While Motor II has a larger magnetizing reactance, which contributes to a higher efficiency, it also has larger rotor and stator resistances, leading to reduced efficiency. In the end, the efficiencies of the two motors align closely.

# Chapter 3

# Cryogenic Tests

After conducting motor tests at room temperature, we started doing the tests in liquid nitrogen.
From the mathematical point of view there are no differences with respect to the previous tests. The only things to care about regard the experimental setup.
First of all is necessary to find a closed environment in which to put the motor and fill it with liquid nitrogen.


Figure 3.1: Liquid nitrogen storage cylinder

Secondly, normal bearings can not be used in cryogenic temperature because the grease inside, useful to reduce friction, freezes. It is therefore necessary to use special bearings. However, the easiest and cheapest solution is to put the bearings in a bowl full of diluent (see Figure 3.2) for some hours in order to remove all the grease.

Figure 3.2: Grease removal process from the bearings

After running tests on the motor submerged in liquid nitrogen, ice formations appear (Figure 3.3). It's essential to let them melt and then ensure the motor is completely dried to remove any residual water, harmful to the bearings.

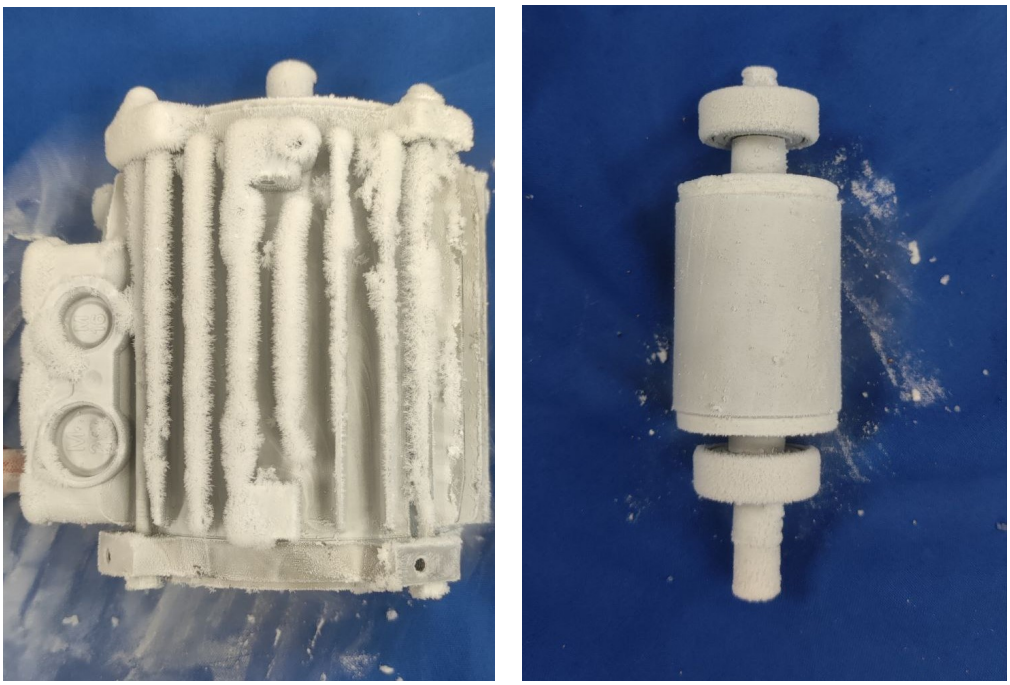

Figure 3.3: Ice formations on the motor after removing from LN2

## 3.1 No-load and Locked Rotor Test

The mathematical procedure for the no-load and locked rotor tests in cryogenic conditions is exactly the same of the one described in Sections 2.4 and 2.5 for ambient conditions.

### 3.1.1 No-load Cryogenic Test

In Figure 3.4 we can see the very simple setup for the no-load cryogenic test.

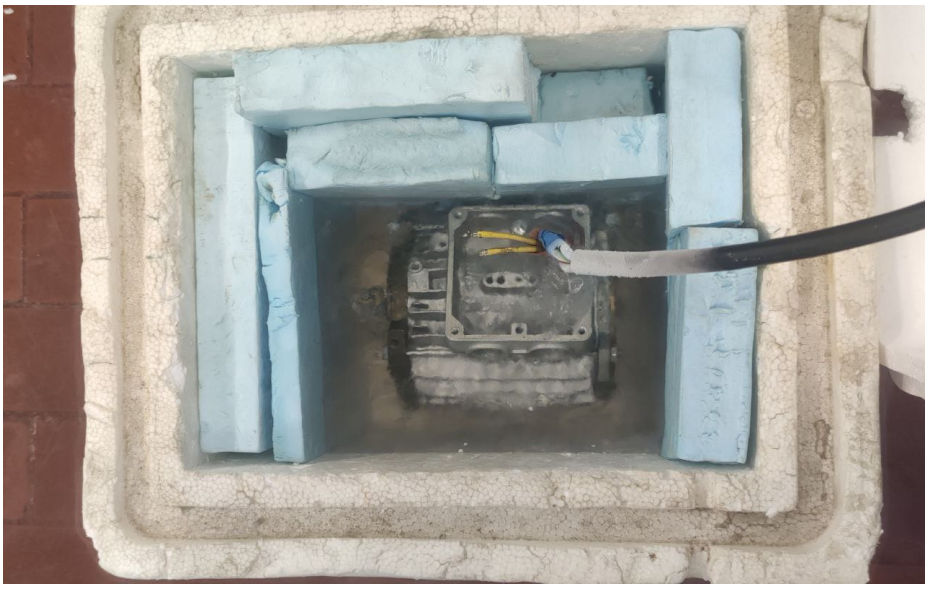

Figure 3.4: No-load test setup in cryogenic conditions

First of all we put the motor inside the polystyrene box and then we poured the liquid nitrogen inside. When LN2 is poured into the box with the motor, a significant amount evaporates. It is therefore necessary to wait and pour more liquid nitrogen until no more bubbles appear, indicating that the system has reached thermal equilibrium. As an additional check, the stator resistance is measured, which, empirically, should be about 8 times lower than the resistance at room temperature.
During the initial test phase, we observed some issues with the motor. Even though at ambient conditions everything worked properly, once submerged in liquid nitrogen it was unable to rotate and produced an unusual noise. The motor operated in what appeared to be a locked rotor condition, causing a rapid increase in current. This forced us to stop the test. We tried to increase the current up to about three times its nominal value and suddenly the motor started rotating briefly for some seconds before stopping again. Firstly, We identified two possible solutions to solve the problem: changing the bearings and checking all the stator phase wires, re-soldering and re-insulating the connections. We did again the test, but it seemed that nothing changed. We then hypothesized a mechanical issue: given the motor's small airgap, there was a possibility that the rotor might come into contact with the stator due to material contraction at cryogenic temperatures and a potential misalignment. We

then proceeded to smooth the rotor using sandpaper while it rotated in the lathe (Figure 3.5).

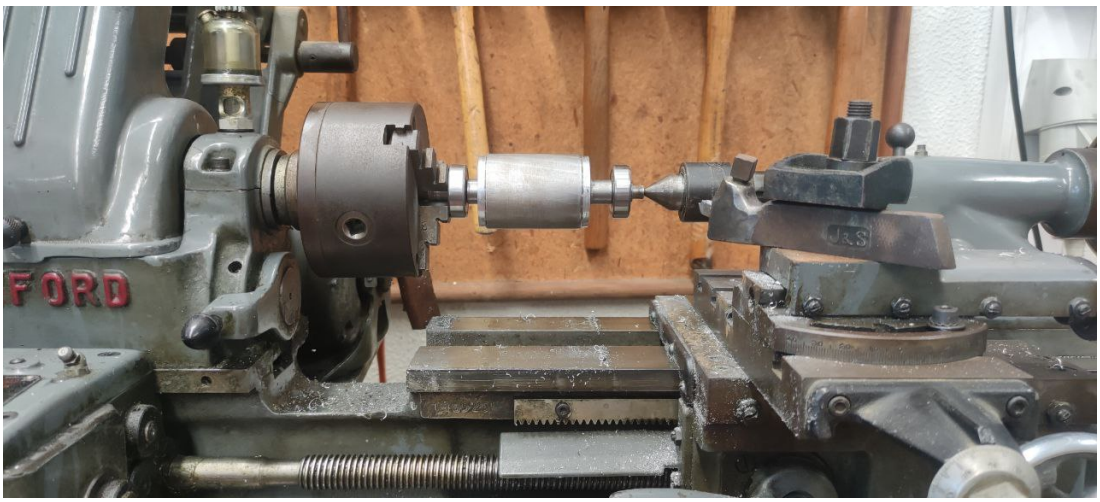


Figure 3.5: Rotor surface smoothing using the sandpaper

After the rotor smoothing, the motor could finally rotate. However, for a certain range of voltage the machine experienced excess vibrations due to some resonance behaviour. For high and low values of voltage, this resonance was attenuated. Therefore, some outliers were visible on the experimental results, and were removed from the fitting (Figure 3.6). The first two points have been also excluded, considering them representative of the mechanical losses.

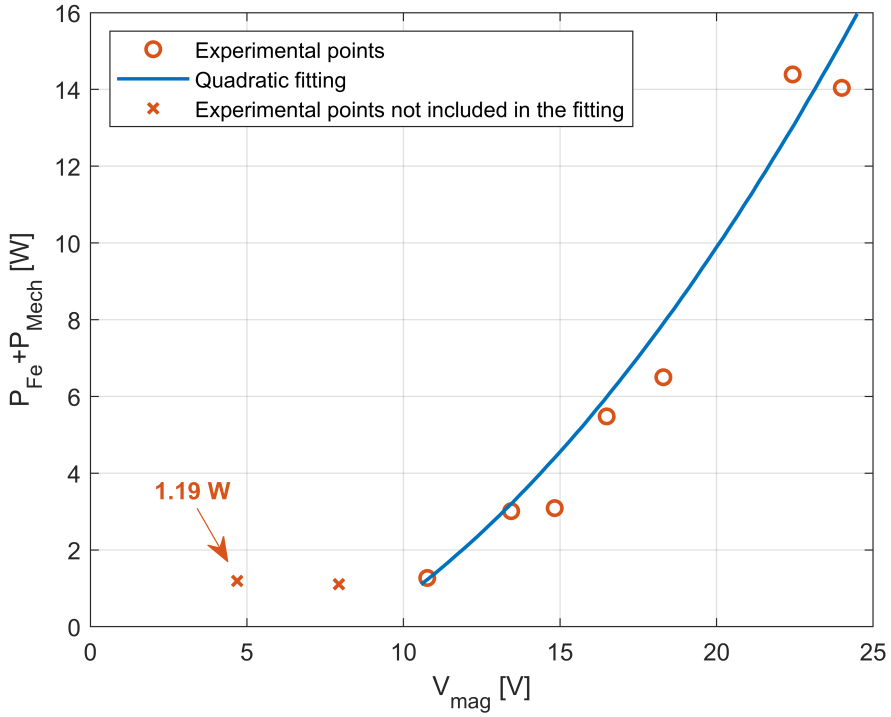


Figure 3.6: No-load cryogenic test: mechanical and iron losses as a function of the magnetizing voltage

The same observations can be applied to the following plot that shows the reactive power.

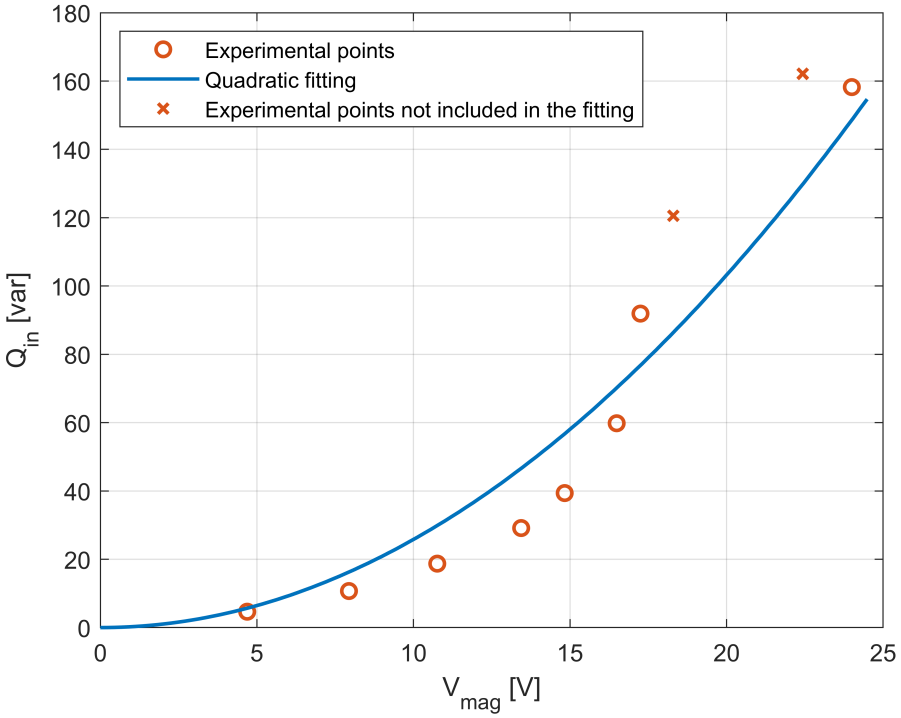


Figure 3.7: No-load cryogenic test: reactive power as a function of the magnetizing voltage

Again, as at ambient conditions, it is possible to find the values of the iron losses resistance and magnetizing reactance using the Equations 2.6 and 2.7,

### 3.1.2 Locked Rotor Cryogenic Test

The locked rotor setup, shown in Figure 3.8, is very similar to the no-load one in Figure 3.4. Since the torque is very low, the rotor can be blocked using a pliers.

Figure 3.8: Locked rotor test setup in cryogenic conditions

Figures 3.9 and 3.10 show the active power and the reactive power as a function of the stator current. Performing a quadrating fitting with Equations 2.12 and 2.13, it is possible to extract the equivalent circuit longitudinal parameters.
The good alignment of the experimental data with the quadratic fit indicates that the test was successful and the measurements were accurate.

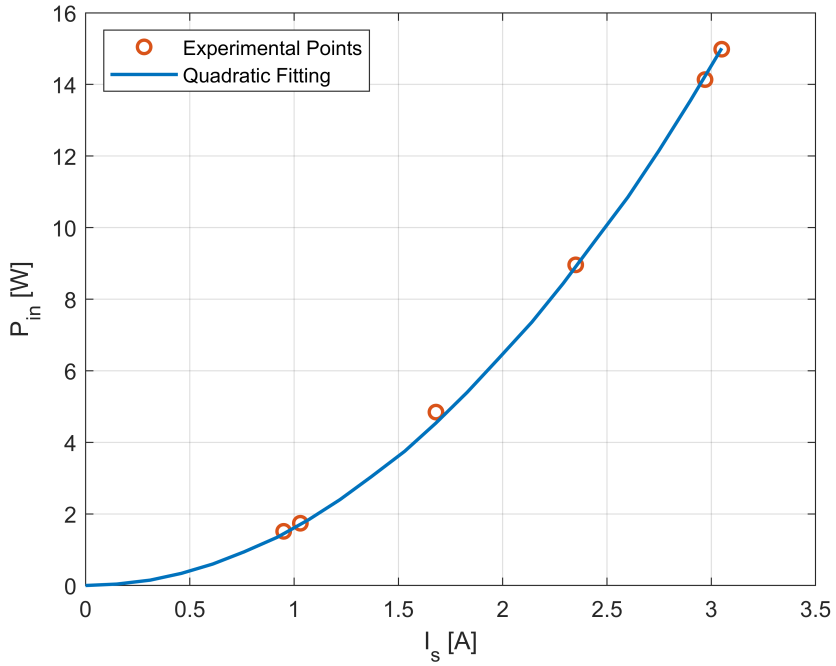


Figure 3.9: Locked rotor cryogenic test: input active power as a function of the stator current

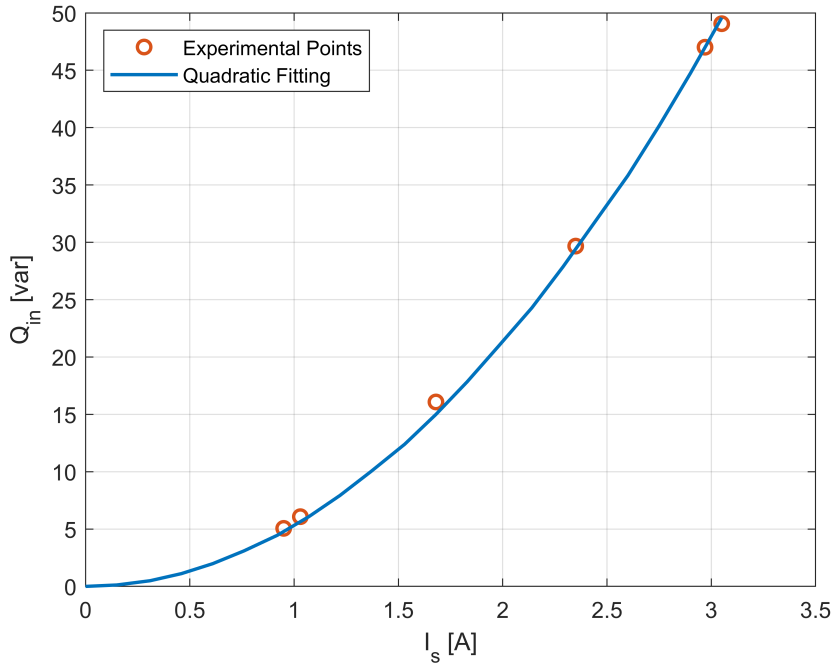


Figure 3.10: Locked rotor cryogenic test: input reactive power as a function of the current

### 3.1.3 Results

The results of the no-load and locked rotor cryogenic tests are shown in Table 3.1. They are compared with those of the same motor obtained at ambient temperature.

The variation is intended to be from ambient to cryogenic.

| | Motor II (MUT) Ambient | | Motor II (MUT) Cryogenic | | Variation |
|---|---|---|---|---|---|
| Equivalent iron losses resistance | 111.11 | Ω | 98.48 | Ω | -11.4% |
| Equivalent magnetizing reactance | 11.21 | Ω | 11.63 | Ω | +3.75% |
| Stator resistance | 1.150 | Ω | 0.150 | Ω | -86.9% |
| Rotor resistance | 1.316 | Ω | 0.382 | Ω | -71.0% |
| Stator reactance | 0.827 | Ω | 0.886 | Ω | +4.7% |
| Rotor reactance | 0.827 | Ω | 0.886 | Ω | +4.7% |
| Mechanical losses | 0.79 | W | 1.19 | W | +50.6% |

Table 3.1: Comparison of the equivalent circuit parameters of Motor II (MUT) in ambient and cryogenic conditions

The results are consistent with those anticipated in Table 1.1 concerning the reduction in resistance and the increase in iron and mechanical losses.

Regarding the inductance, the well known formula for its calculation, starting from the geometry, is the following:

$$L = \frac{N^2}{\mathcal{R}} = N^2 \cdot \frac{\mu S}{l} \tag{3.1}$$

Where $\mathcal{R}$ is the reluctance of the magnetic path. In [27, 28] a decrease in the magnetic permeability was observed: for a 50 Hz frequency the difference is typically of the order of magnitude of 5%-10% from 298 K to 77 K. Therefore, since the geometries do not change in cryogenic conditions, a decrease in the inductance is expected. However the variation strongly depends on the material and we do not have the magnetic characterization of the iron core of our induction motor under test.
In our tests, we observed a rise in the inductances. This discrepancy might come from measurement errors (since the absolute values are small) or inaccuracies in parameter estimation, as we used standards typically suited for larger machines operating at room temperature.

## 3.2 Load Cryogenic Test

For the load test, a similar structure as the one in Figure 2.16 has been used. The motor is coupled with the DC generator and secured to the wooden panel through four screws.
Two horizontal metal brackets and another wooden board have been added to support the polystyrene box containing the liquid nitrogen. The box has two holes: one for the motor shaft to pass through, and the other to insert the liquid nitrogen after the motor has been

coupled.
The setup is shown in Figure 3.11.

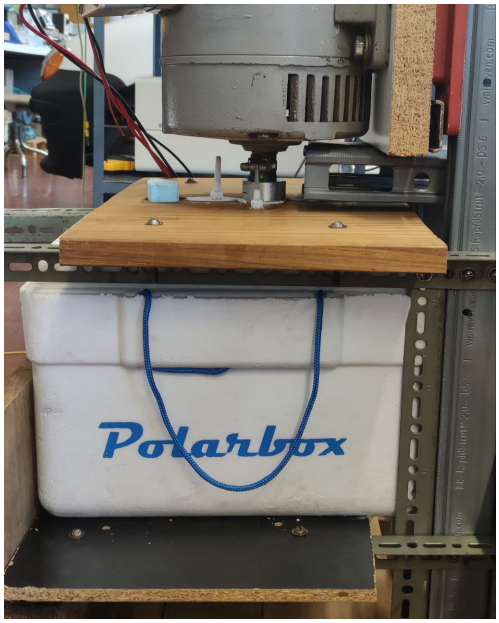


Figure 3.11: Experimental setup for the cryogenic load test

Figure 3.12 shows the induction motor coupled with the DC generator immediately after the load test. After immersion in liquid nitrogen, a mist begins to form when exposed to the air.

Figure 3.12: Mist emerging from the induction motor removed from liquid nitrogen

### 3.2.1 Results

#### Torque vs speed cryogenic characteristics

In Figure 3.13 we can see the experimental points obtained from the load test.
The analytical blue curve is derived from Equation 2.29. This curve, however, doesn't align closely with the data. Therefore, a more complex model, which considers the geometry of the machine and the skin effect, has been introduced [6]. This results in the red curve that is overlapped with the data.

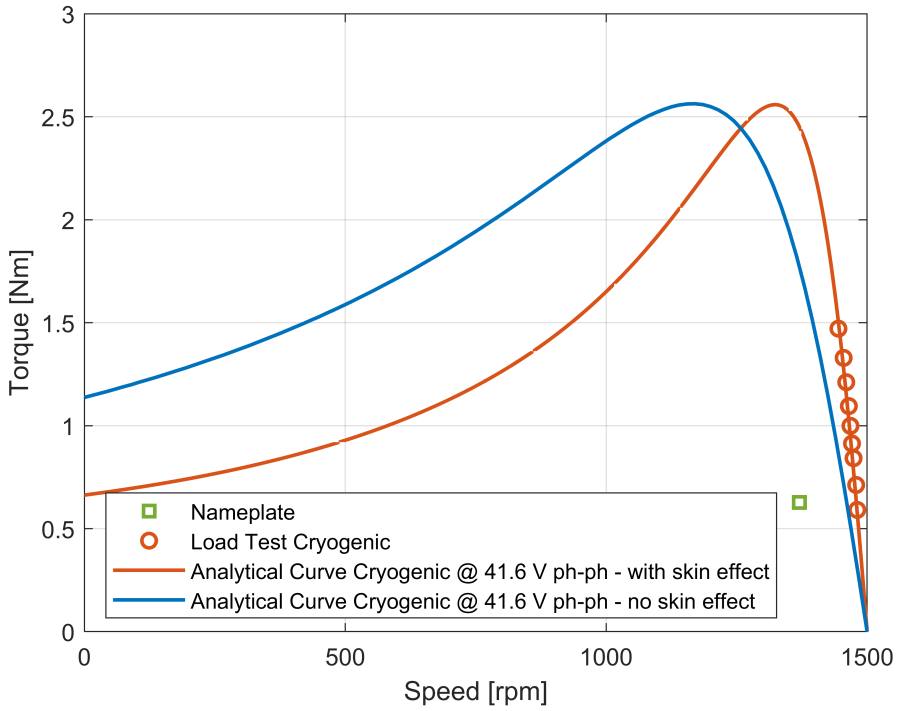


Figure 3.13: Skin effect in the speed vs torque plot in cryogenic conditions

The skin effect refers to the phenomenon where AC current tends to concentrate near the surface of a conductor. As the frequency increases, the effective depth at which the current flows decreases. The skin depth $\delta$ is defined as the depth below the conductor surface at which the current density falls to $1/e \sim 37\%$ of the surface current density.

$$\delta = \sqrt{\frac{2\rho}{\omega\mu}} \tag{3.2}$$

Where:

- $\rho$ is the resistivity of the material at a given temperature
- $\omega$ is the angular frequency of the alternating current
- $\mu$ is the magnetic permeability of the material

The skin effect has influence on both inductances and resistances. The main impact, however, is on the rotor resistance and especially in cryogenic conditions since the resistivity is lower and therefore the skin depth $\delta$ is lower.

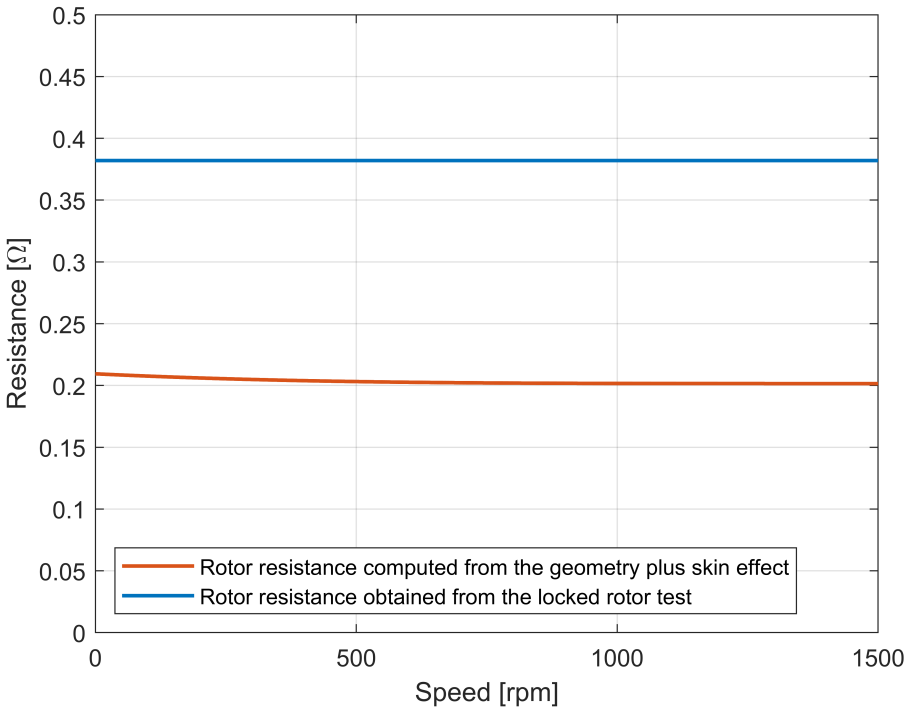


Figure 3.14: Influence of the skin effect on the rotor resistance

Figure 3.14 shows in blue the fixed rotor resistance obtained by the locked rotor test while in red the rotor resistance computed starting from the geometry of the machine and taking into account the skin effect. We can see that the skin effect cause an increase of the resistance (+3.9%) especially at low speed because the slip increase and the frequency of the electrical phenomena induced in the rotor is higher (50 Hz at zero speed if powered from the grid). The blue curve in Figure 3.14 has been used to obtain the blue curve in Figure 3.13 and the same for the red curves.

Now we are going to explain how the rotor resistance was estimated. The final formula is the following [29, 30]:

$$R'_{r,ac} = K_{rs}\left(K_r \cdot \frac{\rho_{Al} L_{bar}}{S_{bar}} + (2K_{ring}) \cdot \frac{\rho_{Al} L_{ring}}{S_{ring}} \cdot \frac{1}{2N_{bars}\sin^2\left(p \cdot \pi / N_{bars}\right)}\right) \tag{3.3}$$

Where:

- $\rho_{Al}$: Resistivity of aluminum.
- $L_{bar}$: Length of the rotor bar.
- $S_{bar}$: Cross-sectional area of the bar. associated with the second ring.

- $L_{ring}$: Length of the end ring. It is the circumference of the midline of the annular crown.
- $S_{ring}$: Cross-sectional area of the end ring.
- $N_{bars}$: Number of rotor bars.
- $p$: Pole pairs of the motor.
- $K_{rs}$: It is the constant that allows referring the rotor resistance to the stator. The formula is the following:

$$K_{rs} = \frac{3}{N_{bars}}(Z_{ph} \cdot k_{w1})^2 \tag{3.4}$$

  Where $Z_{ph}$ is the equivalent number of conductors in series per phase and $k_{w1}$ is the first harmonic winding factor.
- $K_r$: It is the coefficient that accounts for the skin effect in the bars. The coefficient $K_r$ is evaluated as the ratio between AC losses and DC losses as described hereafter. Let us consider a generic shape for the rotor bar as in Figure 3.15.

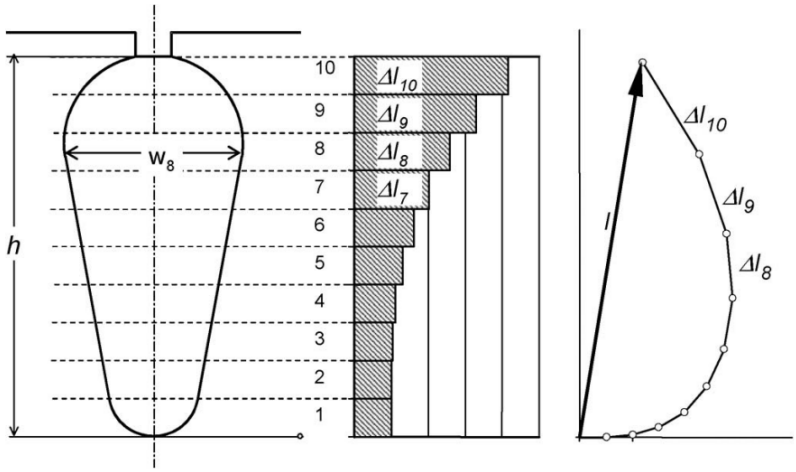


Figure 3.15: Current distribution in the slot layers and related phasor diagram

The total height of the bar, $h$, is divided in N segments of height $\Delta h_k$ each one with a width of $w_k$. For each layer we can calculate the electrical resistance as follow:

$$R_k = \rho_{Al} \cdot \frac{l_{stack}}{\Delta h_k \cdot w_k} \tag{3.5}$$

Being $l_{stack}$ the axial length of the rotor lamination stack.
On the basis of the mutual-inductance matrix between the layer, it is possible to find the following phasor relation:

$$\Delta\bar{I}_k = \frac{w_k}{w_{k-1}}\Delta\bar{I}_{k-1} + j\beta(\Delta\bar{I}_1 + \Delta\bar{I}_2 + \cdots + \Delta\bar{I}_{k-1}) \tag{3.6}$$

Where:

$$\beta = 2\pi f \left(\frac{\mu_0}{\rho_{Al}}\right)\left(h^2/N^2\right) \tag{3.7}$$

It is possible to consider an arbitrary current in the first layer (i.e., $\Delta\bar{I}_1 = 1 + j0\ A$). Therefore, once determined the current for each layer $\Delta\bar{I}_k$, we can calculate the total current of the bar as:

$$I = |\bar{I}_1 + \bar{I}_2 + ... + \bar{I}_k + \bar{I}_N| \tag{3.8}$$

The DC losses can now be evaluated as follows:

$$P_{DC} = \sum_{k=1}^{N}\left(R_k \cdot \left(I \cdot \frac{w_k \cdot \Delta h_k}{A_{bar}}\right)^2\right) \tag{3.9}$$

Where:

$$A_{bar} = \sum_{k=1}^{N}(w_k \cdot \Delta h_k) \tag{3.10}$$

Basically, we did the assumption that the current density is homogeneous throughout the entire bar. As a result, the total current is distributed proportionally across each layer's section. Visually, this is equivalent to segmenting the magnitude of the phasor $I$ into N parts through scalar summation. However, when calculating the AC losses, we take into account the real phasorial current, denoted as $\Delta\bar{I}_k$, for each layer. The formula is the following:

$$P_{AC} = \sum_{k=1}^{N}\left(R_k \cdot |\Delta\bar{I}_k|^2\right) \tag{3.11}$$

Finally the skin effect coefficient is:

$$K_r(f) = \frac{P_{AC}}{P_{DC}} \tag{3.12}$$

It has to be noticed that it is a function of the frequency of the electrical phenomena induced in the rotor. Consequently, $K_r$ varies in function of the rotor speed and, therefore, the slip.

- $K_{ring}$: It is the skin effect coefficient for the end rings. For the computation, the skin effect formula for rectangular conductors was used [31].

$$K_{ring} = \frac{w_{ring}}{\delta} \cdot \frac{\sinh\left(2w_{ring}/\delta\right) + \sin\left(2w_{ring}/\delta\right)}{\cosh\left(2w_{ring}/\delta\right) - \cos\left(2w_{ring}/\delta\right)} \tag{3.13}$$

Where:

$$\delta = \sqrt{\frac{2 \cdot \rho_{Al}}{2\pi f \mu_0}} \tag{3.14}$$

While $w_{ring}$ is the height of the annular ring.

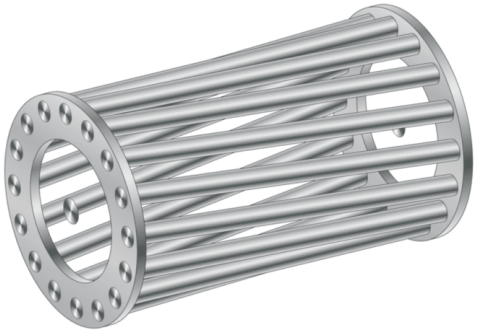

Figure 3.16: Squirrel cage rotor design

### Speed vs efficiency cryogenic characteristics

Regarding the efficiency, the analytical curve and the load test data are very close.

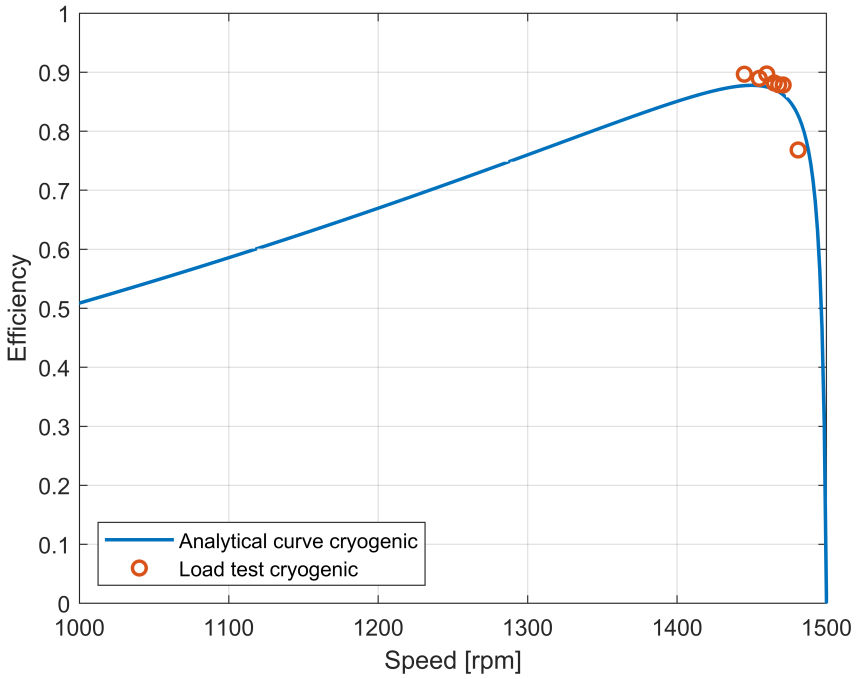


Figure 3.17: Speed vs efficiency cryogenic characteristics of Motor II (MUT)

## 3.3 Room vs Cryogenic Temperature Comparison

### 3.3.1 Torque and Power

Figure 3.18 shows the comparison between the ambient and cryogenic tests. Both the experimental results and the analytical curves are represented.

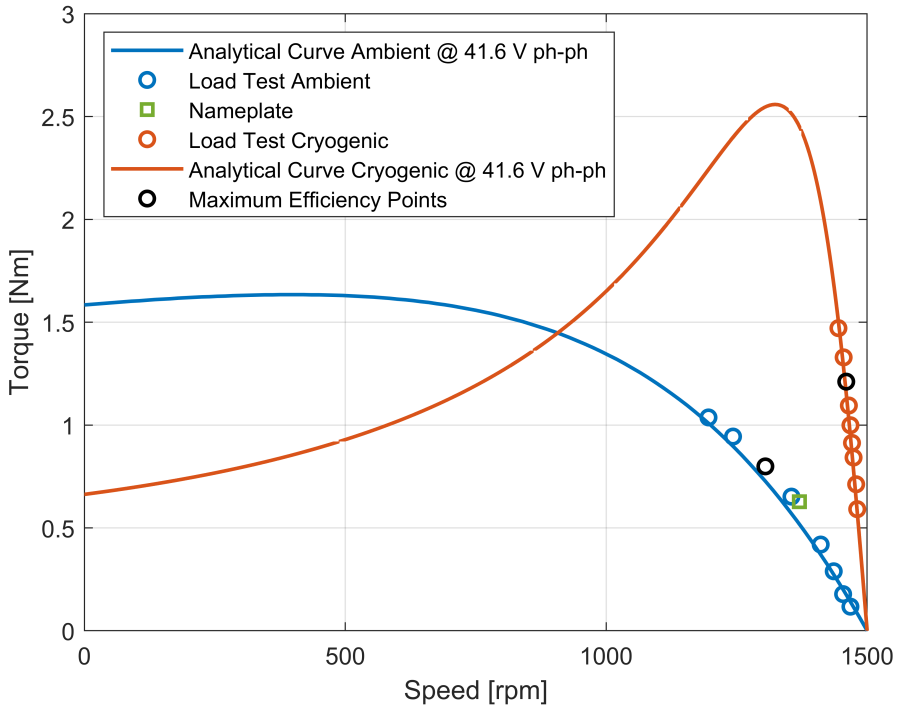


Figure 3.18: Speed vs torque characteristics comparison between room and cryogenic temperature for Motor II (MUT)

Three main difference can be noticed:
1) The starting torque in cryogenic temperature is lower
2) The slope of the linear region in cryogenic temperature is higher
3) The peak of the torque in cryogenic temperature is higher

These changes must be due to the change in stator and rotor resistance between room and cryogenic temperature. The following graph will help us analyze better what we said.

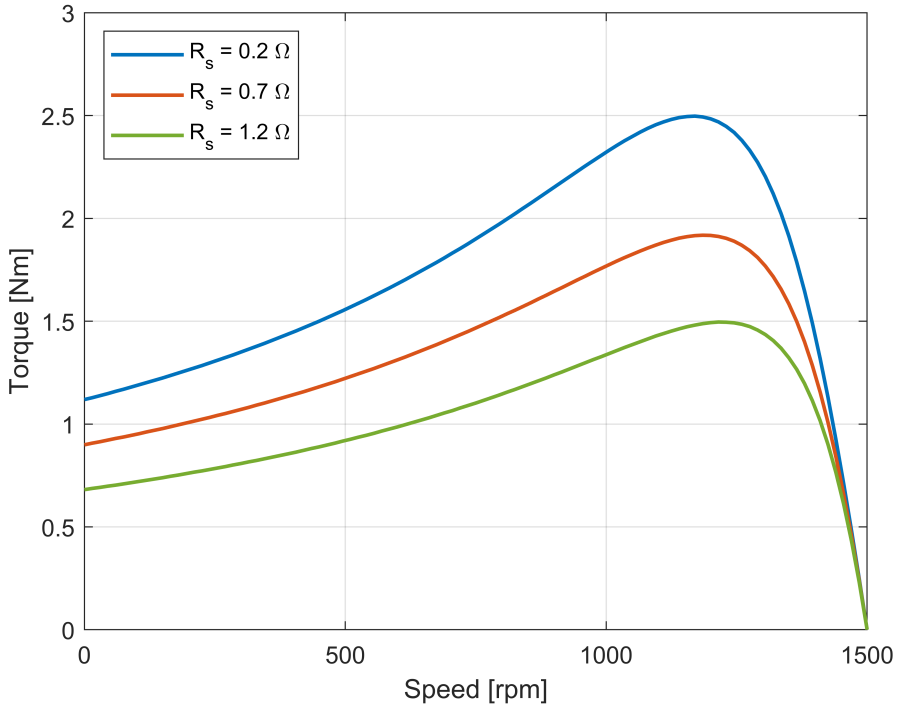


Figure 3.19: Speed vs torque characteristics as function of the stator resistance

In Figure 3.19, a parametric variation of the stator resistance was made. All the other parameters were kept constant. It is clear that if the resistance is lower (lower temperature) then the starting torque increases and most of all the peak of the torque increases, while the slope of the linear region remains constant.

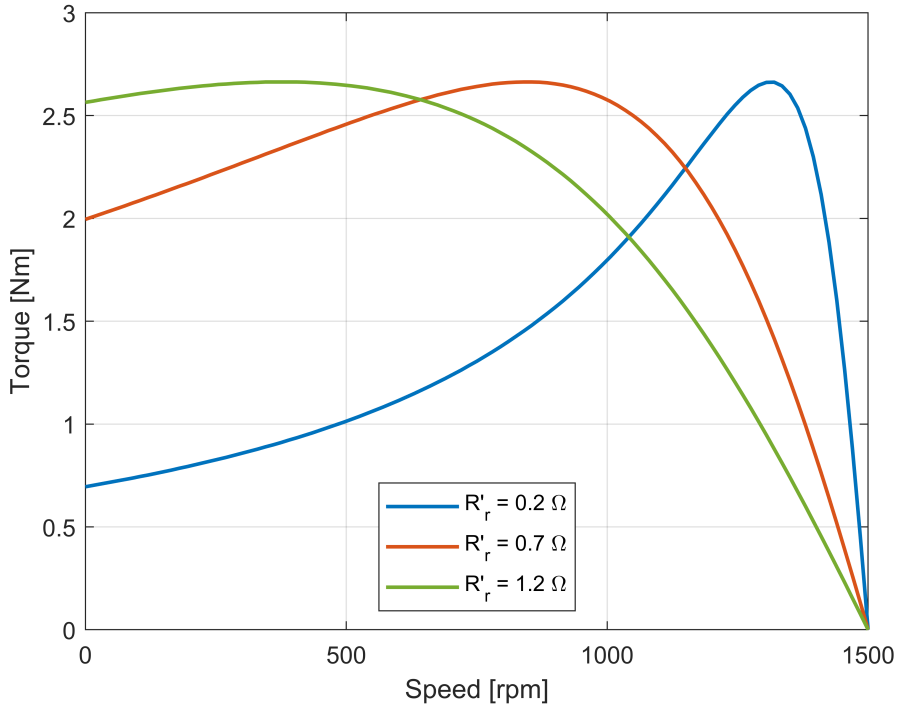


Figure 3.20: Speed vs torque characteristics as function of the rotor resistance

Similarly, in Figure 3.20, a parametric variation of the rotor resistance was made. We can see that the peak of the torque remains constant while the slope of the linear region increases for lower temperature. Moreover the variation in the starting torque due to rotor resistance is even higher with respect to the variation due to stator resistance that we observed in Figure 3.19 and has an opposite trend.

Let us now examine the results from a quantitative point of view. Three different torque comparisons were made in Table 3.2.

| | Ambient test | Cryogenic test | Variation |
|---|---|---|---|
| Maximum experimental torque [Nm] | 1.037 | 1.471 | +41.9% |
| Torque @ maximum efficiency [Nm] | 0.799 | 1.211 | +51.6% |
| Torque @ same output power [Nm] | 0.646 | 0.590 | -8.67% |

Table 3.2: Comparison of torque values between ambient and cryogenic test

- The maximum experimental torque can be seen in Figure 3.18. For ambient and cryogenic temperature it was obtained respectively with a stator current of 3.82A and 4.76A. It must be pointed out, however, that the maximum current in cryogenic conditions could be further increased (and consequently the torque);
- The experimental points at maximum efficiency are coloured in black in Figure 3.18. They were found watching at the speed vs efficiency plot in Figure 3.22;

- The third comparison was conducted at an output power nearly identical to the nominal ambient value, as illustrated in Figure 3.21. For the cryogenic torque, we used the precise experimental data point. For the ambient torque, we performed a linear interpolation between the two points closest to 91.6W.

In all the three comparisons we can notice a significant increase in torque performance from ambient to cryogenic operations. In the final scenario, a reduced torque indicates that, for the same output power, the motor operates at a higher speed. Given that the volume of the machine is proportional to its torque ( $T \propto D^2L$), maintaining the same output power under cryogenic conditions permits the use of a more compact motor, resulting in weight and space savings.

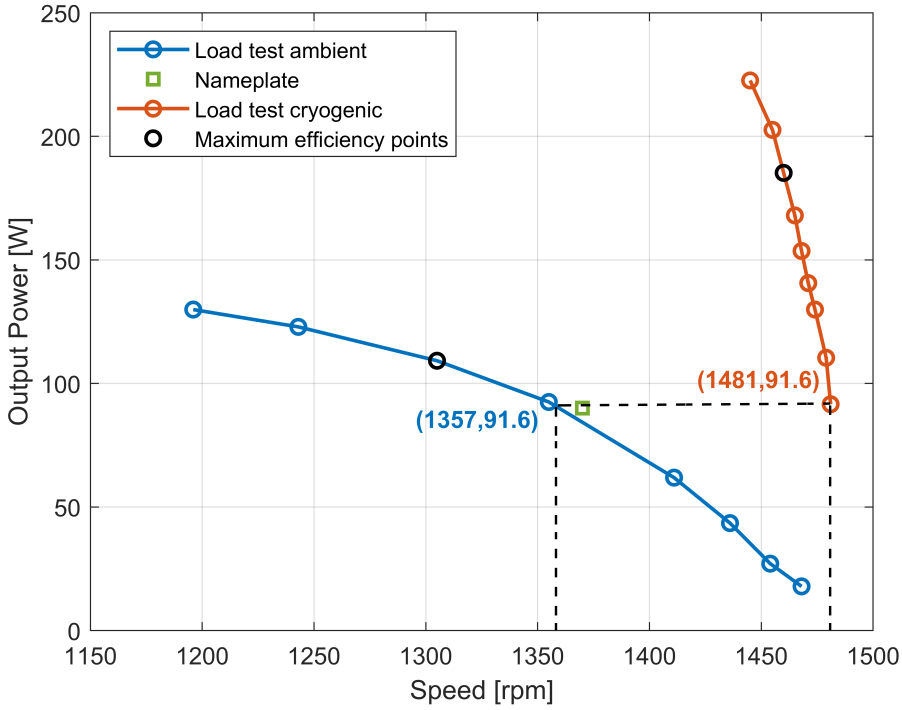


Figure 3.21: Speed vs output power characteristics comparison between room and cryogenic temperature for Motor II (MUT)

Regarding the power, a big increase in performance (Table 3.3) can be obtained in cryogenic conditions. The points with the maximum efficiency (black dots in Figure 3.21) have been considered for the comparison.

| | Ambient test | Cryogenic test | Variation |
|---|---|---|---|
| Maximum Output Power [W] | 129.9 | 222.6 | +71.4% |
| Output Power @ maximum efficiency [W] | 109.2 | 185.2 | +69.6% |

Table 3.3: Comparison of output power values between ambient and cryogenic tests

### 3.3.2 Efficiency

Figure 3.22 shows the comparison of the speed vs efficiency characteristics in ambient and cryogenic conditions for the motor under test.

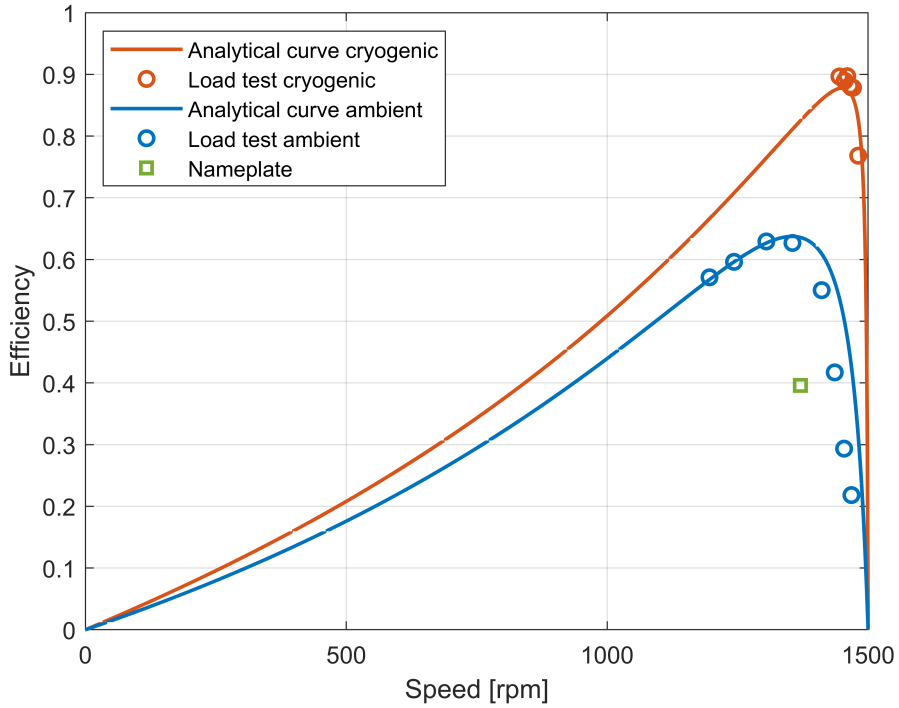


Figure 3.22: Speed vs efficiency characteristics comparison between room and cryogenic temperature for Motor II (MUT)

The maximum efficiency has seen a significant increase, as shown below:

| | Ambient test | Cryogenic test | Variation |
|---|---|---|---|
| Maximum Efficiency | 62.9% | 89.7% | +26.8% |

Table 3.4: Comparison of efficiency values between ambient and cryogenic tests for Motor II (MUT)

Despite the significant increase in efficiency, an important observation has to be done: it is not the optimum choice to design a motor for ambient conditions and then make it work in cryogenic to improve its efficiency. Even though efficiency might go up, to get the best performance, the motor should be properly designed for cryogenic conditions.
From Figure 3.18, we can see that if we move horizontally at nominal torque up to the red cryogenic curve, we do not reach the maximum efficiency point. The same for Figure 3.21 if we move horizontally at nominal power. Finally, also in Figure 3.22, we can see that the maximum efficiency points occur at different speeds.

## 3.4 Comparison with a Similar Motor

Below are summarized the parameters of the equivalent circuit for both 90W motors and for both operating conditions, ambient and cryogenic. As we can see, the variation of the parameters is very similar for the two motors, giving validity to the conducted tests.

| | Motor I Ambient | | Motor I Cryogenic | | Variation |
|---|---|---|---|---|---|
| Equivalent iron losses resistance | 116.4 | Ω | 104.3 | Ω | -10.4% |
| Equivalent magnetizing reactance | 7.33 | Ω | 7.24 | Ω | -1.2% |
| Stator resistance | 1.10 | Ω | 0.175 | Ω | -84.1% |
| Rotor resistance | 0.914 | Ω | 0.240 | Ω | -73.4% |
| Stator reactance | 0.532 | Ω | 0.532 | Ω | +0.0% |
| Rotor reactance | 0.532 | Ω | 0.532 | Ω | +0.0% |
| Mechanical losses | 1.96 | W | 3.83 | W | +95.4% |

Table 3.5: Variation of the parameters of 90W Motor I from ambient to cryogenic conditions

| | Motor II Ambient | | Motor II Cryogenic | | Variation |
|---|---|---|---|---|---|
| Equivalent iron losses resistance | 111.11 | Ω | 98.48 | Ω | -11.4% |
| Equivalent magnetizing reactance | 11.21 | Ω | 11.63 | Ω | +3.75% |
| Stator resistance | 1.150 | Ω | 0.150 | Ω | -86.9% |
| Rotor resistance | 1.316 | Ω | 0.382 | Ω | -71.0% |
| Stator reactance | 0.827 | Ω | 0.886 | Ω | +4.7% |
| Rotor reactance | 0.827 | Ω | 0.886 | Ω | +4.7% |
| Mechanical losses | 0.79 | W | 1.19 | W | +50.6% |

Table 3.6: Variation of the parameters of 90W Motor II (MUT) from ambient to cryogenic conditions

Table 3.7, shows the variation of the parameters for the two 90W motor and also for a 550W induction motor tested in our lab. The iron losses resistance and the stator and rotor resistances experienced almost the same variation. It is interesting to notice that the iron losses had a very similar variation independently of the power rating of the machine.
The biggest concern is on the reactances: the negative variation for the 550W motor supports the thesis pointed out in Section 3.1.3.
Regarding the mechanical losses, despite the difference between the two 90W motors, we could assume that the variation, from ambient to cryogenic, increase for bigger machines.

| | 90W Motor I | 90W Motor II (MUT) | 550W Motor |
|---|---|---|---|
| Equivalent iron losses resistance: | -10.4% | -11.4% | -10.6% |
| Equivalent magnetizing reactance: | -1.2% | +3.75% | -2.6% |
| Stator resistance: | -84.1% | -86.9% | -84.0% |
| Rotor resistance: | -73.4% | -71% | -60.3% |
| Stator reactance: | +0.0% | +4.7% | -7.6% |
| Rotor reactance: | +0.0% | +4.7% | -7.6% |
| Mechanical losses: | +95.4% | +50.6% | +146% |

Table 3.7: Comparison of the equivalent circuit parameters variation

Figure 3.23 shows the speed vs torque characteristics comparison in cryogenic conditions for Motor I and Motor II. As we can see, the experimental data of the two motors are quite overlapped even if Motor I was made to work at a higher current: 158% of its nominal current for Motor I against 112% of its nominal current for Motor II.
Regarding the analytical curve, the peak torque for Motor II is much lower than Motor I and it is shifted to the right towards higher rotor speed and therefore lower slip: this is mainly due to the difference between the leakage reactances, that are higher for Motor II. It is well known, in fact, that the maximum torque and the maximum torque correspondent slip are inversely proportional to the leakage reactances:

$$T_{max} \propto \frac{1}{X_{\sigma s} + X'_{\sigma r}} \ , \ s_{T_{max}} \propto \frac{1}{X_{\sigma s} + X'_{\sigma r}} \tag{3.15}$$

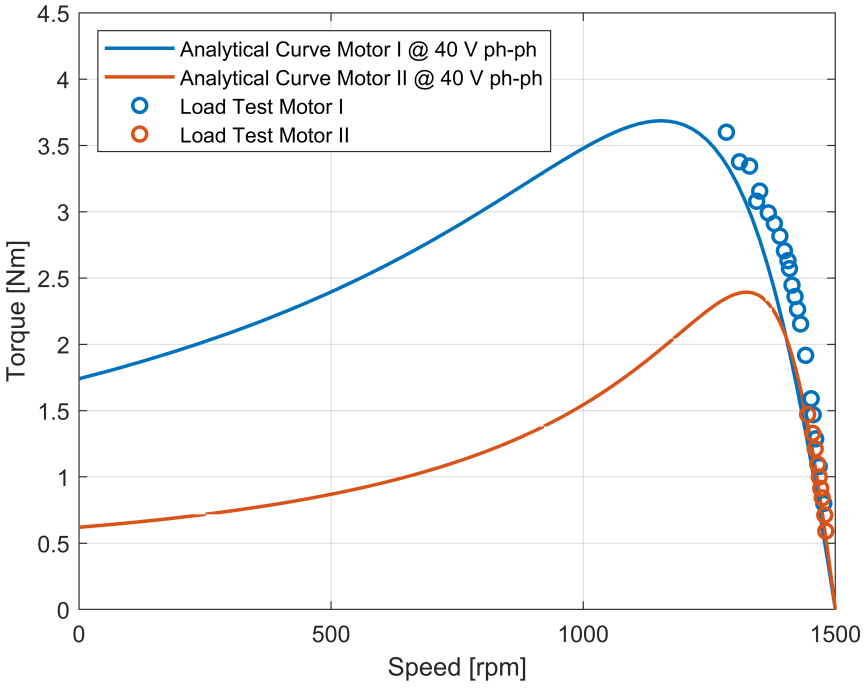


Figure 3.23: Speed vs torque characteristics comparison between Motor I and Motor II

Regarding the speed vs efficiency plot in Figure 3.24, both the analytical curves and the experimental points are overlapped.

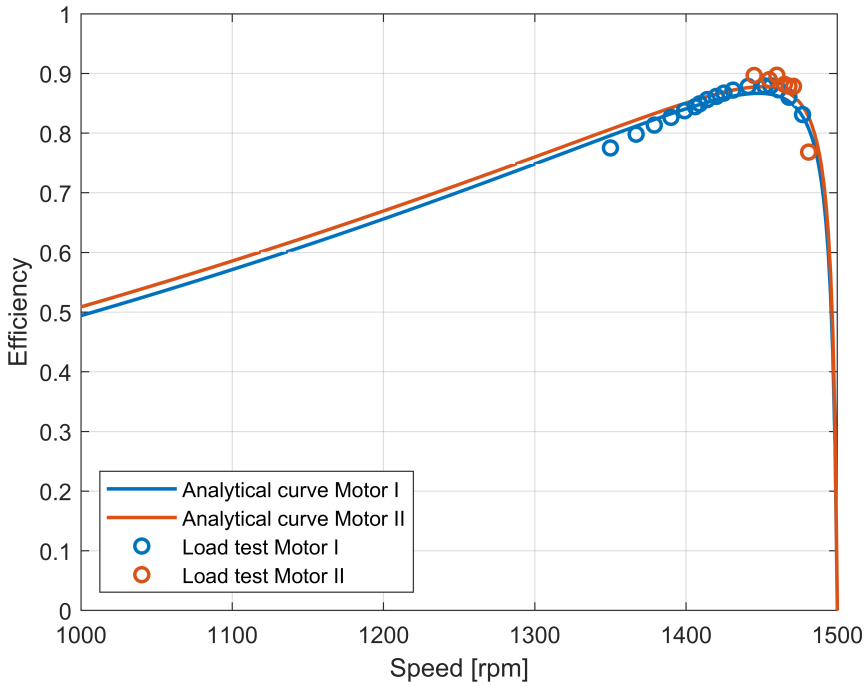


Figure 3.24: Speed vs efficiency characteristics comparison between Motor I and Motor II (MUT)

In conclusion, a comparison of the cryogenic performance of the three induction motors is made in Table 3.8. Regarding the efficiency, all the motors saw a considerable increase, reaching values around $85\% \div 90\%$ in cryogenic conditions. In terms of torque and output power, the 90W Motor I experienced an excellent increase, while for the 90W Motor II and the 550W Motor the increase was lower, but still very high.

| | 90W Motor I | 90W Motor II (MUT) | 550W Motor |
|---|---|---|---|
| Maximum efficiency | +22.2% | +26.8% | +20.6 % |
| Torque @ maximum efficiency | +171% | +51.6% | +84% |
| Output power @ maximum efficiency | +189% | +69.6 % | +96% |

Table 3.8: Comparison of performance variation from ambient to cryogenic conditions

# Chapter 4

# Additional Load Losses

## 4.1 Theoretical Overview

The efficiency of an electric motor can be determined by one of the following equations:

$$\eta_{direct} = \frac{P_{m,out}}{P_{e,in}} \tag{4.1}$$

$$\eta_{indirect} = \frac{P_{e,in} - P_d}{P_{e,in}} \tag{4.2}$$

$$\eta_{indirect} = \frac{P_{m,out}}{P_{m,out} + P_d} \tag{4.3}$$

The direct method (Equation 4.1) involves measuring the actual inputs and outputs directly. The indirect method calculates the efficiency by mean of the power losses, either subtracting them from the electrical input power (Equation 4.2) or adding them to the mechanical output power (Equation 4.3). Therefore, using the second method, it is essential to take into account all kind of losses. In Section 4.1.2 the details of the direct and indirect methods will be further discussed.
The conventional losses are typically divided into: stator and rotor joule losses, iron losses and mechanical losses. There are, however, other non conventional losses that the standard procedure of performance calculation do not take into account. These additional losses are called stray load losses.

### 4.1.1 Physical Phenomena Underlying Stray Load Losses

Stray load losses can be classified into those due to theoretical imperfections, and those due to industrial imperfections [32]. The first group exists by nature, while the second group can be attenuated by improving the processes of manufacturing of squirrel cage rotors.
The physical origins of the stray load losses in induction machines are related to the following:

- The magnetic property limitations of iron that lead to saturation at load current;

- The geometrical structure (slots, winding, air gap) around the active region of the machine.
- Cross-bar currents due to imperfect insulation of the squirrel cage rotor bars.

After listing some of the physical causes for the stray load losses, their possible consequences will be analyzed.
Regarding fundamental frequency components:

- Skin effect in the stator winding;
- Eddy current losses in end region copper, steel and other metallic part owing to end region leakage fluxes.

Regarding high frequency components:

- Skin effect in the rotor cage, harmonic rotor currents due to the third space harmonic caused by iron saturation;
- Teeth pulsation losses in the rotor and the stator caused by the distortion of the air gap flux density distribution due to the slot openings;
- Losses in the stator winding due to harmonic currents and circulating currents in delta connected stator windings due to the third space; harmonic caused by iron saturation
- Iron losses in the stator core due to the third space harmonic caused by the distortion of the field distribution due to iron saturation [33].

### 4.1.2 Efficiency and Losses Estimation According to Different Standards

Regarding the direct efficiency measurement, the IEEE 112-A standard specify the procedure to follow. As far as the indirect efficiency measurement method is concerned, there are different possibilities to estimate the losses:

- Total losses estimation through calorimetric method. This methods compute all the losses together, both the conventional ones and the stray load losses;
- Segregation of the losses and indirect measurement of the stray load losses according to IEEE 112-B;
- Segregation of the losses and direct measurement of the stray load losses according to IEEE 112-E;

- Segregation of the losses and assumed value of the stray load losses according to IEEE 112-E1. The following table shows the stray load losses as a percentage of the output power.

| Machine rating [kW] | Stray load losses |
|---|---|
| 1 - 90 | 1.8 % |
| 91 - 375 | 1.5 % |
| 376 - 1850 | 1.2 % |
| >1850 | 0.9 % |

Table 4.1: Assigned values in stray load losses in IEEE 112

The National Electrical Manufacturers Association (NEMA) recommends 1.2 % for induction motors rated less than 1850 kW, and 0.9 % for ratings 1850 kW and above.
Although many measurement estimation method are proposed in literature [34–36], as well as in IEEE-E, we will refer to the IEEE 112-B standard that defines the stray load losses as the difference between the total measured losses and the conventional losses, as in Equation 4.4 [37].

$$P_{Residual} = P_{Electrical} - P_{Mechanical} - P_{Conventional} \tag{4.4}$$

Where:

$$P_{Conventional} = P_{Js} + P_{Jr} + P_{Iron} + P_{Mech} \tag{4.5}$$

It has to be noticed that $P_{Residual}$ is the raw unsmoothed residual loss. To obtain the real stray load losses, a linear regression analysis, plotting $P_{Residual}$ values against the square of the torque, $T^2$, must be done.

$$P_{Residual} = A \cdot T^2 + B \tag{4.6}$$

Where A (slope) and B (offset) are constant coefficients. The offset B, which can be positive or negative, is removed to obtain the corrected stray load loss.

$$P_{Stray} = A \cdot T^2 \tag{4.7}$$

However, the intercept B should be considerably smaller ($< 50\%$) than the stray load losses at rated torque, otherwise the measurements may be erroneous.
Finally, the standard only applies to machines operating at ambient temperature.

## 4.2 Experimental Results at Cryogenic Temperature

As stated in the previous section, the IEEE 112-B was used, considering therefore the segregation of the losses and indirect measurement of the stray load losses.

The conventional losses of Equation 4.5 were computed according to the IEC 60034-2-1 standard as follows:

- $P_{js} = 3R_sI_s^2$ where $R_s$ is the stator resistance of the equivalent circuit and $I_s$ is the stator phase current;
- $P_{iron} = f(U_m^2)$ as a function of the magnetizing voltage;
- $P_{jr} = (P_{in} - P_{js} - P_{iron}) \cdot s$ where $s$ is the slip;
- $P_{mech} = P_{mech0} \cdot (1-s)^{2.5}$ where $P_{mech0}$ are the mechanical losses at zero voltage found in the no load test.

The result, in cryogenic conditions, for the motor under test is the following:

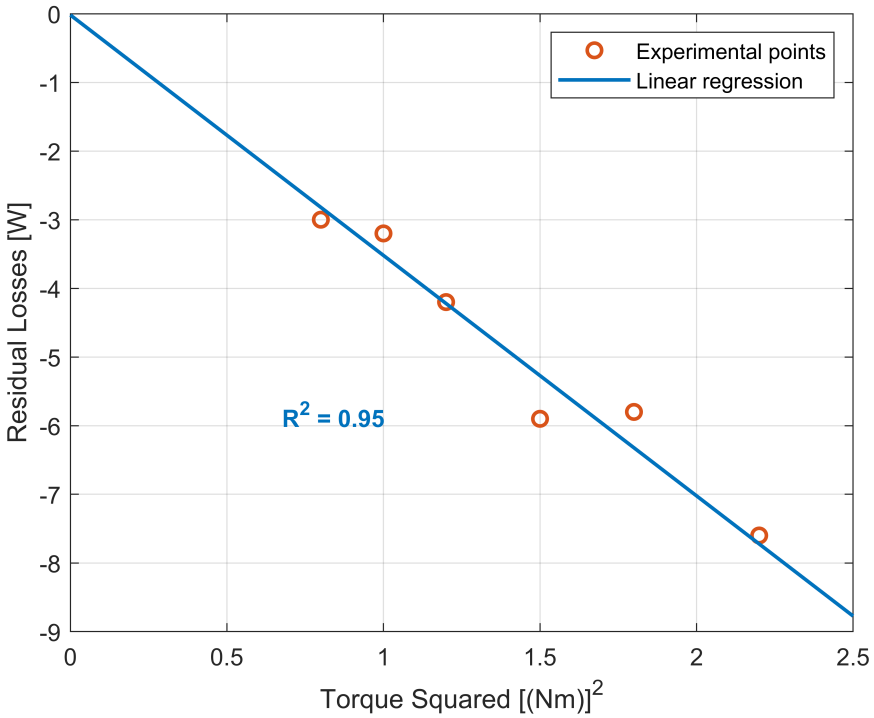


Figure 4.1: Residual load losses Motor II (MUT)

It is important to underline that the coefficient of determination $R^2$ of the linear regression is very sensitive to the measurement accuracy. In particular, if a point is very far from the linear trend, some measurement errors are certainly present. In other words, it is possible to consider the stray-load loss curve as a quality factor of the performed measurement.
The negative slope of the residual losses is something unexpected. It is important to point out, however, that the IEEE 112-B standard considers motor with rated power greater then 1 kW in ambient conditions. Our analysis is focused on a 90 W motor in cryogenic conditions.

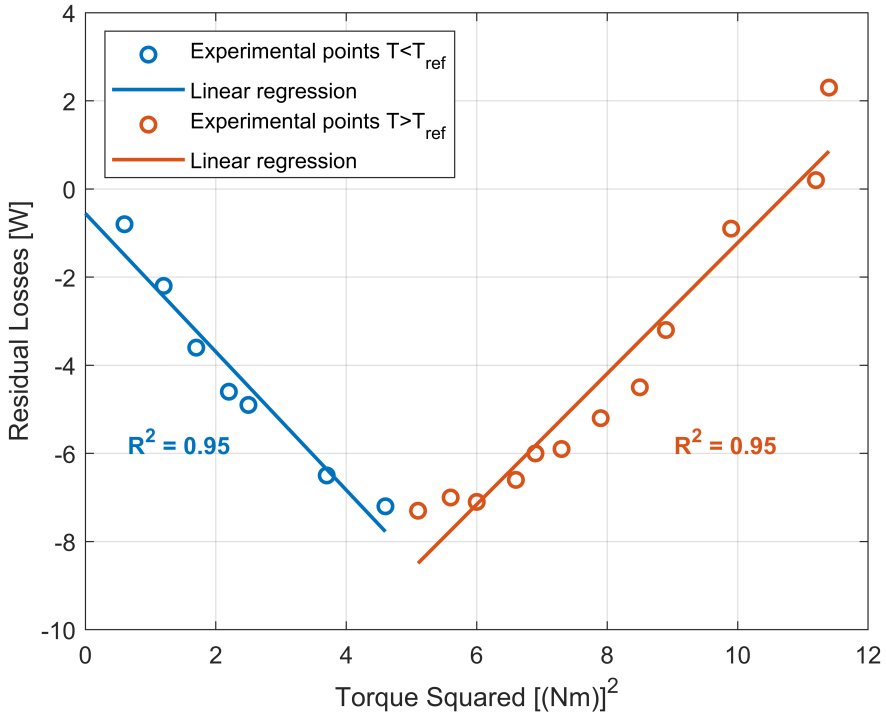


Figure 4.2: Residual load losses Motor I

Regarding the Motor I, the same negative slope can be seen in Figure 4.2 for torque values lower than the reference torque. $T_{ref}$ is the torque value at maximum efficiency in cryogenic conditions.
For torque values higher than $T_{ref}$, a positive slope has been observed.

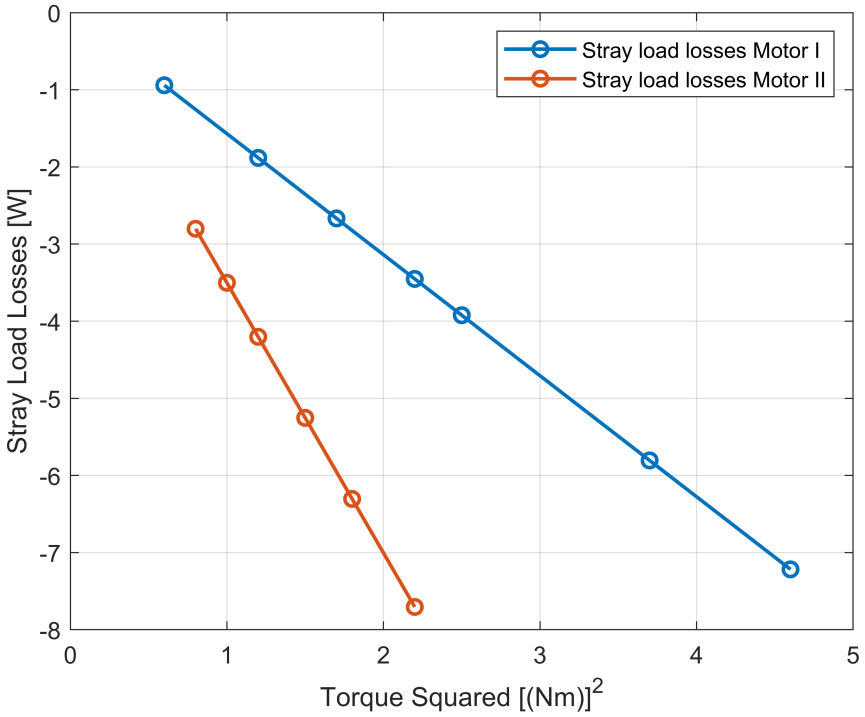


Figure 4.3: Stray load losses comparison between Motor I and Motor II (MUT)

Figure 4.3 shows the comparison of the stray load losses, obtained after removing the offset of the linear regression, of Motor I (with $0 < T < T_{ref}$) and Motor II in cryogenic conditions. Considering the absolute value of the stray load losses, they represent 2.00 % of the reference output power at maximum efficiency for Motor I and 2.65 % for Motor II. These values have the same order of magnitude of the one showed in Table 4.1.
However, from the slope, it can be seen that the Motor II has more stray load losses than Motor I. This is expected because of its more irregular behavior under cryogenic conditions. As already stated in Section 3.1, in fact, we experienced some problems with the no-load test and it had to be repeated several times.

# Chapter 5

# Conclusions and Future Works

## 5.1 Conclusions

In this thesis, the performances of a conventional three phase 90W induction motor have been evaluated by comparing its operation at ambient temperature to its behavior when submerged in liquid nitrogen. The effects of cryogenic conditions on the overall performance and its equivalent electric circuit parameters have been examined. To validate our results, they have been compared with data from a prior study on a comparable 90W induction motor.

The study involved conducting no-load and locked rotor tests on the induction motor to determine its equivalent circuit parameters in ambient and cryogenic conditions. Using these parameters, an analytical model has been used to calculate torque and efficiency. In parallel, a test bench for the motor under load has been set up in both conditions, coupling it with a DC generator. The experimental data obtained was then compared with the theoretical predictions, and the results were consistent.

As expected from literature, the motor in LN2 had an increase in mechanical losses of +95.4 % with respect to room temperature. Also iron losses increased by +10.4 % due to the higher conductivity of the core in cryogenic conditions.

However, significant improvements of the performance have been observed in cryogenic environment. The torque at maximum efficiency increased by +51.6 %, while the power at maximum efficiency increased by +69.6 %.

All in all, the maximum efficiency increased from 62.9 % to 89.7 %, thus meaning that even a small motor can achieve a very high efficiency by mean of cryogenic cooling.

Concerning the stray load losses under cryogenic conditions, a negative slope trend as a function of squared torque can be observed. This deviates from standard expectations, even if it is worth noting that such standards typically apply to larger motors operating at ambient temperatures. The observed results, however, are confirmed by the analysis of the other similar motor. Based on our analysis, stray load losses constitute 2.65 % of the output power at peak efficiency in cryogenic conditions.

In conclusion, the results of this thesis affirm that despite several drawbacks, primarily the

complexity of the cooling system and the high costs, cryogenic electric motors are highly promising. They offer significant improvements in performance metrics such as efficiency, torque and power density, making them the best solution for application demanding high power with limited space requirements, as the aeronautical sector.

## 5.2 Future Works

Since the output power and torque of the motor under test were measured through the coupled DC generator, the tests could be repeated using a torque sensor to obtain more accurate data.
Moreover the negative variation of the reactances from ambient to cryogenic conditions should be further investigated, as well as the negative slope of the stray load losses.
Finally, it would be interesting to use an inverter to power the machine and observe how the parameters and the performance of the motor change with changes in frequency.

# Bibliography


[1] Julio R Gómez et al. "Assessment criteria of the feasibility of replacement standard efficiency electric motors with high-efficiency motors". In: *Energy* 239 (2022), p. 121877.

[2] Paul Waide and Conrad U Brunner. "Energy-efficiency policy opportunities for electric motor-driven systems". In: (2011).

[3] Fabrizio Marignetti and Guido Rubino. "Perspectives on Electric Machines with Cryogenic Cooling". In: *Energies* 16.7 (2023), p. 2994.

[4] André Baeten et al. "Parameterized pre-dimensioning of a winding-integrated cryogenic hydrogen cooling system in an axial flux motor for ship propulsion systems". In: *The 33rd International Ocean and Polar Engineering Conference*. OnePetro. 2023.

[5] Marco Biasion et al. "A comparison of cryogenic-cooled and superconducting electrical machines". In: *2021 IEEE Energy Conversion Congress and Exposition (ECCE)*. IEEE. 2021, pp. 4045–4052.

[6] Luís FD Bucho et al. "Experimental assessment of cryogenic cooling impact on induction motors". In: *IEEE Transactions on Energy Conversion* 37.4 (2022), pp. 2629–2636.

[7] Luís FD Bucho et al. "Losses analysis of induction motors under ambient and cryogenic conditions". In: *2022 IEEE Energy Conversion Congress and Exposition (ECCE)*. IEEE. 2022, pp. 01–07.

[8] Marco Biasion et al. "Iron Loss Characterization in Laminated Cores at Room and Liquid Nitrogen Temperature". In: *2022 IEEE Energy Conversion Congress and Exposition (ECCE)*. IEEE. 2022, pp. 1–8.

[9] Wai-Kwong Kwok et al. "Vortices in high-performance high-temperature superconductors". In: *Reports on Progress in Physics* 79.11 (2016), p. 116501.

[10] Jin Wang et al. "Comparison study of superconducting wind generators with HTS and LTS field windings". In: *IEEE transactions on applied superconductivity* 25.3 (2014), pp. 1–6.

[11] Russell Shively. "Submerged cryogenic motor materials development". In: *IEEE Electrical Insulation Magazine* 19.3 (2003), pp. 7–11.

[12] David C Larbalestier. “The road to conductors of high temperature superconductors: 10 years do make a difference!” In: *IEEE transactions on applied superconductivity* 7.2 (1997), pp. 90–97.

[13] Jesse H Redmond and Fred W Bott. “Development of cryogenic electric motors”. In: *SAE Transactions* (1964), pp. 257–268.

[14] Marco Biasion et al. “Design and Analysis of High-Speed Induction Machines for Submerged Cryogenic Pumps”. In: *2023 IEEE International Electric Machines & Drives Conference (IEMDC)*. IEEE. 2023, pp. 1–7.

[15] L Dlugiewicz et al. “Electrical motor for liquid gas pump”. In: *International Symposium on Power Electronics, Electrical Drives, Automation and Motion, 2006. SPEEDAM 2006.* IEEE. 2006, pp. 311–316.

[16] Hui Min Kim et al. “Design of cryogenic induction motor submerged in liquefied natural gas”. In: *IEEE Transactions on Magnetics* 54.3 (2017), pp. 1–4.

[17] Oleksandr Zaporozhets, Volodymyr Isaienko, and Kateryna Synylo. “Trends on current and forecasted aircraft hybrid electric architectures and their impact on environment”. In: *Energy* 211 (2020), p. 118814.

[18] Francisco Ferreira da Silva, João FP Fernandes, and Paulo Jose da Costa Branco. “Barriers and challenges going from conventional to cryogenic superconducting propulsion for hybrid and all-electric aircrafts”. In: *Energies* 14.21 (2021), p. 6861.

[19] Joseph Benzaquen, JiangBiao He, and Behrooz Mirafzal. “Toward more electric powertrains in aircraft: Technical challenges and advancements”. In: *CES Transactions on Electrical Machines and Systems* 5.3 (2021), pp. 177–193.

[20] Junhan Zhao et al. “An Overview of High Specific Power Electrical Machines and Drives Technologies for Electrified Aircraft”. In: *2022 IEEE Energy Conversion Congress and Exposition (ECCE)*. IEEE. 2022, pp. 1–8.

[21] Ludovic Ybanez et al. “ASCEND: The first step towards cryogenic electric propulsion”. In: *IOP Conference Series: Materials Science and Engineering*. Vol. 1241. 1. IOP Publishing. 2022, p. 012034.

[22] Dev Paul. “A history of electric ship propulsion systems [history]”. In: *IEEE Industry Applications Magazine* 26.6 (2020), pp. 9–19.

[23] Jan Fredrik Hansen and Frank Wendt. “History and state of the art in commercial electric ship propulsion, integrated power systems, and future trends”. In: *Proceedings of the IEEE* 103.12 (2015), pp. 2229–2242.

[24] David Torrey et al. “Superconducting synchronous motors for electric ship propulsion”. In: *IEEE Transactions on Applied Superconductivity* 30.4 (2020), pp. 1–8.

[25] Haran Karmaker et al. “High-power dense electric propulsion motor”. In: *IEEE transactions on industry applications* 51.2 (2014), pp. 1341–1347.

[26] "IEEE Standard Test Procedure for Polyphase Induction Motors and Generators". In: *IEEE Std 112-2017 (Revision of IEEE Std 112-2004)* (2018), pp. 1–115.

[27] B Jankowski et al. "Influence of cryogenic temperature on magnetic properties of soft magnetic composites". In: *Powder Metallurgy* 57.2 (2014), pp. 155–160.

[28] Xiaoze Pei et al. "Magnetic characterization of soft magnetic cores at cryogenic temperatures". In: *IEEE Transactions on Applied Superconductivity* 29.5 (2019), pp. 1–6.

[29] Aldo Boglietti, Andrea Cavagnino, and Mario Lazzari. "Computational algorithms for induction-motor equivalent circuit parameter determination—Part I: Resistances and leakage reactances". In: *IEEE Transactions on Industrial Electronics* 58.9 (2010), pp. 3723–3733.

[30] Aldo Boglietti, Andrea Cavagnino, and Mario Lazzari. "Computational algorithms for induction motor equivalent circuit parameter determination—Part II: Skin effect and magnetizing characteristics". In: *IEEE Transactions on Industrial Electronics* 58.9 (2010), pp. 3734–3740.

[31] Zakari Maddi, Djamel Aouzellag, and Toufik Laddi. "Influence of the skin effect and the form of slot on the starting characteristics of induction motor squirrel cage". In: *Recent Advances in Mechanics, Mechatronics and Civil, Chemical and Industrial Engineering* (2015), pp. 125–129.

[32] SSL Chang. "Physical Concepts or Stray Load Loss in Induction Machines [includes discussion]". In: *Transactions of the American Institute of Electrical Engineers. Part III: Power Apparatus and Systems* 73.1 (1954), pp. 10–12.

[33] Adisa Abdul-Ganiya Jimoh. "Stray load losses in induction machines". PhD thesis. 1986.

[34] Emmanuel B Agamloh. "An evaluation of induction machine stray load loss from collated test results". In: *IEEE transactions on Industry Applications* 46.6 (2010), pp. 2311–2318.

[35] Hansjörg Köfler. "Stray load losses in induction machines. A review of experimental measuring methods and a critical performance evaluation". In: *International Conference on Renewable Energy and Power Quality (ICREPQ).* Vol. 390. 2003, pp. 2423–2430.

[36] M Aoulkadi et al. "Experimental Determination of stray load losses in cage induction machines". In: (2011).

[37] Aldo Boglietti et al. "International standards for the induction motor efficiency evaluation: a critical analysis of the stray-load loss determination". In: *38th IAS Annual Meeting on Conference Record of the Industry Applications Conference, 2003.* Vol. 2. IEEE. 2003, pp. 841–848.

# Appendix

## Skin Effect Calculation

```
function [Rr_dc,Rr_ac1,Rr_ac2, KL, Kr, Kr_rect] = ...
skin_effect_cage(f,rho_al)
nhu0=4*pi*1e-7;

global x_slot
global y_slot

%% Rr' DC
% rho_cu=1.68e-8*(1+0.00404*(75-20));
% rho_al=2.65e-8*(1+0.00390*(75-20));
% %v2
% rho_al=2.65e-8*(225+75)/(225+20);

global N % Number of conductors in series per slot
global kw1
global s
global pp
global Zph

tau_i=0.0096;
Lcore=0.055;
gamma=atan(tau_i/Lcore);
Lbar=0.055/cos(gamma);
% delta=sqrt(2*rho_al/(2*pi*104*4*pi*1e-7));
Abar=20.44e-6*cos(gamma);
Nbars=22;
Br=2*pi/Nbars;
Da=(42e-3-7e-3);
Aa=9e-3*7e-3;
wa=sqrt(Aa);
Kr=1;
Rr=Kr*rho_al*Lbar/Abar+2/(4*Nbars*sin(Br/2)^2)*rho_al*pi*Da/Aa;
Krs=3/Nbars*(Zph*kw1)^2;
Rr_dc=Krs*Rr;

delta=sqrt(2*rho_al/(2*pi*f*nhu0));
```

```
% Kr=h/delta*(sinh(2*h/delta)+sin(2*h/delta))/(cosh(2*h/delta)-...
cos(2*h/delta));
[Kr, KL]=Kr_calc(b,h,Lbar,f,s,1/rho_al);

% rectangular
beta=sqrt((s*2*pi*f*nhu0)/(2*rho_al));
csi=beta*h*length(b);
Kr_rect=csi*(sinh(2*csi)+sin(2*csi))/(cosh(2*csi)-cos(2*csi));
% ------------
Kr_ring1=wa/delta*(sinh(2*wa/delta)+sin(2*wa/delta))/(cosh(2*wa/delta)-...
cos(2*wa/delta));
Kr_ring2=wa/delta*(sinh(2*wa/delta)+sin(2*wa/delta))/(cosh(2*wa/delta)-...
cos(2*wa/delta));
% ----------------
Ra=rho_al*pi*Da/Aa;
Rr1=Kr*rho_al*Lbar/Abar+2*Ra/(4*Nbars*sin(Br/2)^2);
Rr2=Kr*rho_al*Lbar/Abar+Kr_ring1*Kr_ring2*2*Ra/(4*Nbars*sin(Br/2)^2);

Rr_ac1=Krs*Rr1;
Rr_ac2=Krs*Rr2;

Rslot=Krs*Kr*rho_al*Lbar/Abar;
Rring=Krs*2/(4*Nbars*sin(Br/2)^2)*rho_al*pi*Da/Aa;

end
```

## Kr Calculation

```
function [Kr, KL] = Kr_calc(b,h,lstack,f,s,cond_al)
% function Kr = Kr_calc(b,h,lstack,f,s,cond_al)
nhu0=4*pi*1e-7;
% f=50;
w=2*pi*f;
% s=1;
n=length(b);

% cond_al=1/(4.37e-8);
```

```
R=1/cond_al*lstack./(b.*h); % resistances
L=nhu0*lstack*h./b; % inductances

Ib=1; % initial value
I=zeros(1,n);
I(1)=Ib/n;

I2=zeros(1,n);
I2(1)=Ib/n;
for i=2:n
    I(i)=R(i-1)/R(i)*I(i-1)+1i*s*w*L(i-1)/R(i)*sum(I(1:i-1));
%     delta=w*(nhu0*cond_al)*(sum(h)^2/(n^2));
%     I2(i)=b(i)/b(i-1)*I2(i-1)+1i*delta*sum(I2(1:i-1));
end

Ib_f=abs(sum(I));
% Ib2_f=abs(sum(I2));

% losses AC
Pac=sum(abs(I).^2.*R);
% Pac2=sum(abs(I2).^2.*R);

% losses DC
Abar=sum(b.*h);
I_dc=Ib_f*b.*h/Abar;
%
% I2_dc=Ib2_f*b.*h/Abar;

Pdc=sum(abs(I_dc).^2.*R);
% Pdc2=sum(abs(I2_dc).^2.*R);

Kr=Pac/Pdc;
% Kr2=Pac2/Pdc2
% end

sumLI=0;
sumLIdc=0;
for j=1:n
    It=0;
    for k=1:j
```

```
        It=It+(I(k));
    end
    sumLI=sumLI+L(j)*abs(It)^2;

    It_dc=0;
    for k=1:j
        It_dc=It_dc+(I_dc(k));
    end
    sumLIdc=sumLIdc+L(j)*abs(It_dc)^2;
end

KL=sumLI/sumLIdc;
end
```